**Ubiquitin profiling of lysophagy identifies actin-stabilizer CNN2 as a target of VCP/p97 and uncovers link to HSPB1**

Bojana Kravić [1], Tihana Bionda [2], Alexander Siebert [2], Pinki Gahlot [1], Sophie Levantovsky [2], Christian Behrends [2,*], Hemmo Meyer [1,*#]

[1] *Center of Medical Biotechnology, Faculty of Biology, University of Duisburg-Essen, Essen, Germany*

[2] *Munich Cluster for Systems Neurology (SyNergy), Medical Faculty, Ludwig-Maximilians-Universität München, Feodor-Lynen-Str. 17, 81377 Munich, Germany*

[*] *Corresponding authors:*
*hemmo.meyer@uni-due.de, Christian.Behrends@mail03.med.uni-muenchen.de*

*# Lead contact*

**Summary:**

Lysosomal membrane permeabilization (LMP) is an underlying feature of diverse conditions including neurodegeneration. Cells respond by extensive ubiquitylation of membrane-associated proteins for clearance of the organelle through lysophagy that is facilitated by the ubiquitin-directed AAA-ATPase VCP/p97. Here, we assessed the ubiquitylated proteome upon acute LMP and uncovered a large diversity of targets and lysophagy regulators. They include calponin-2 (CNN2) that, along with the Arp2/3 complex, translocates to damaged lysosomes and regulates actin filaments to drive phagophore formation. Importantly, CNN2 needs to be ubiquitylated during the process and removed by VCP/p97 for efficient lysophagy. Moreover, we identified the small heat shock protein HSPB1 that assists VCP/p97 in extraction of CNN2, and show that other membrane regulators including SNAREs, PICALM, AGFG1 and ARL8B are ubiquitylated during lysophagy. Our data reveal a framework of how ubiquitylation and two effectors, VCP/p97 and HSPB1, cooperate to protect cells from the deleterious effects of LMP.

Keywords: lysophagy, ubiquitin, AAA+ protein, lysosome, autophagy, actin

## Introduction:

Lysosomes are the main degradative organelles of the cell and key signaling platforms. Lysosomal membrane permeabilization (LMP) can therefore compromise cellular homeostasis, and may induce cell death and inflammation (Gomez-Sintes et al., 2016; Yim and Mizushima, 2020). Diverse conditions and agents can cause LMP including pathogens, silica and lysosomotropic drugs as well as oxidative stress, changes in lipid composition or uptake of proteotoxic aggregates associated with neurodegeneration and lysosomal storage diseases (Gabande-Rodriguez et al., 2019; Liu et al., 2020; Logan et al., 2021; Papadopoulos et al., 2020).

To cope with LMP, cells mount a concerted endo-lysosomal damage response (ELDR) (Papadopoulos et al., 2020). One branch triggers the biogenesis of lysosomal components through dissociation of mTOR and activation of TFEB (Jia et al., 2018; Nakamura et al., 2020). In parallel, components of the ESCRT machinery repair damage to the limiting membrane (Radulovic et al., 2018; Skowyra et al., 2018). Presumably when repair fails, damaged lysosomes are cleared by a form of selective macroautophagy, termed lysophagy (Maejima et al., 2013; Yim and Mizushima, 2020). Lysophagy is initiated by the influx of cytosolic galectins such as galectin-3 (Gal3, encoded by LGALS3) that bind luminal beta-galactosides and by ubiquitin ligase components that trigger extensive ubiquitylation of lysosomal proteins (Chauhan et al., 2016; Koerver et al., 2019; Liu et al., 2020; Yoshida et al., 2017). Modification with ubiquitin serves to recruit autophagy receptors such as p62/SQSTM1 and TAX1BP1, which link the damaged lysosome to the LC3-decorated phagophore (Eapen et al., 2021; Koerver et al., 2019; Maejima et al., 2013). Moreover, ubiquitin attracts additional autophagy machinery to promote formation of an autophagosome that can fuse with intact lysosomes for degradation (Fujita et al., 2013).

In addition, ubiquitylation triggers the recruitment of the AAA+-type ATPase p97 (also called VCP) (Papadopoulos et al., 2017). Based on the established ubiquitin-directed segregase activity of p97 (van den Boom and Meyer, 2018; Ye et al., 2017), p97 is thought to bind and extract ubiquitylated factors from the damaged lysosome or the forming phagophore in order to facilitate lysophagy. However, the identity of the p97 targets has remained unknown. Mutations of p97 in humans cause multisystem proteinopathy that features neuronal conditions such as fronto-temporal dementia (FTD), amyotrophic lateral sclerosis (ALS), and Charcot-Marie-Tooth (CMT) disease in addition to inclusion body myopathy and Paget's disease of bone (Al-Obeidi et al., 2018; Watts et al., 2004). Of note, VCP/p97 is critical for maintenance of lysosome homeostasis (Arhzaouy et al., 2019). Moreover, disease-

associated mutations impair p97-driven lysophagy in vitro and damaged lysosomes accumulate in patient tissue (Papadopoulos et al., 2017), suggesting that a compromised response to LMP contributes to the pathogenesis of p97-associated disease.

In this study, we profiled the proteins that are ubiquitylated specifically after lysosome damage. In addition to resident lysosomal proteins, we identified a group of ubiquitylated membrane trafficking factors and other regulators that are recruited to damaged lysosomes and have not been linked to lysophagy. Among them, we identified calponin-2 (CNN2) that assists phagophore formation by regulating actin and is then targeted by ubiquitylation and p97 for timely removal. Notably, we also reveal a link to HSPB1 that, like p97, is associated to neurodegeneration (Vendredy et al., 2020). These findings uncover a mechanistic framework of how ubiquitylation and the ubiquitin effectors, p97 and HSBP1, cooperate to protect cells from the consequences of LMP.

## Results:

### Ubiquitylation proteome after lysosomal damage

In order to gain mechanistic insight into the complex function of ubiquitylation in the endo-lysosomal damage response, we performed ubiquitylation site profiling using quantitative diGly proteomics. Thereto, we combined stable isotope labeling by amino acids in cell culture (SILAC) with immunoaffinity-based enrichment of diGly remnant-containing peptides after tryptic digestion of ubiquitinated proteins. For robust lysosomal damage, we applied the widely used L-Leucyl-L-Leucine methyl ester (LLOMe) that condenses to hydrophobic poly-leucine specifically in late endosomes and lysosomes, and permeabilizes their membranes (Aits et al., 2015; Jia et al., 2018; Maejima et al., 2013; Radulovic et al., 2018; Skowyra et al., 2018; Thiele and Lipsky, 1990; Yoshida et al., 2017). Briefly, human HeLa cells were triple SILAC labeled and treated with LLOMe or vehicle alone for 1 h (**Figure 1A**). Cells were harvested either directly after LLOMe treatment or after an additional 2 h chase following LLOMe washout. This strategy allowed us to monitor ubiquitylation dynamics during progression of the damage response. Cells from the 3 different conditions were lysed under denaturing conditions, and combined in a 1:1:1 ratio. Following protein extraction and proteolytic digestion, tryptic peptides were subjected to sequential anti-diGly immunoprecipitation (IPs) (**Figure 1A**). In triplicate experiments, we quantified a total of 3471 non-redundant diGly sites in 1528 proteins (**Figure 1B, Table S1**). Across the three SILAC comparisons, we identified between 385 and 724 diGly sites (198 - 396 proteins) with log2 (SILAC) ratios ≥1.0 (2-fold increase) in at least two out of three experiments (**Figure 1B**). Pearson's correlation coefficients between 0.70 and 0.98 indicated high reproducibility between biological replicate samples (**Figure 1C**), concomitant with a substantial overlap across the top 20 most increased diGly sites (CNN2_K234, CNN2_K52, CNN2_K134, UPAP2L_K353, CLINT1_K183, DDX3X_K215, PICALM_K570, NUP98_K663, AGFG1_K318) between the acute (medium:light [M:L]) and the progressed (heavy:light [H:L]) response (**Figure 1D)**. Notably, in the same experiment we also quantified protein abundance changes and found that the vast majority of proteins – including candidates with highly regulated sites - remained largely unaltered upon lysosomal damage (**Figure S1A-D)**.

We classified altered diGly sites according to their dynamics into those that were (i) exclusively increased after 1 h (Class I; 30 diGly sites), (ii) increased after 1 and 3 h (Class II; 141 diGly sites), (iii) continuously increased over 3 h (Class III; 187 diGly sites) and (iv) only increased after 3 h (Class IV; 393 diGly sites) (**Figure 1E)**. Functional annotation analysis of increased diGly sites revealed enrichment of transmembrane (TM) proteins in

Class I; of components of SNARE complexes, lysosomal and late endosomal (LE) membranes, multivesicular bodies, exosomal secretion and post-Golgi vesicle transport in Class II as well as the shared terms RNA and $Ca^{2+}$-dependent protein binding, protein stabilization and glycolysis among Class III and IV (**Figure 1F**). A closer look at the number of diGly sites per protein revealed several “hot spot” ubiquitylation targets in Class II (SPG20, CLINT1, TRIM29), Class III (CDK1, DDX3X, ENO1, ANXA1, ANXA2, BZW1, PLIN3) and Class IV (VIM, PPIA, CLF1, CCT2, HNRNPM) (**Figure 1G**). With regard to target localization, we noted that class I diGly sites were exclusively found in the cytosolic tail of TM proteins such as the neurological disease associated proteins SLC1A3 and TMEM106B. In contrast, luminal lysosomal proteins (GLA, PPT1, PPT2) and luminal moieties of membrane proteins (LAMP1, CD63) as well as lysophagy components (LGALS1, LGALS3 (also called Gal3), SQSTM1) mostly carried Class III and Class IV diGly sites.

As for functional categorization, endomembrane trafficking components (VAMP3, VAMP7, VAMP8, VTI1B, RAB7A, STAM, HGS, PDCD6IP/ALIX, ARL8B, SPG20, PICALM, PI4K2A, CLINT1, CAV1, ARFGAP1, AGFG1 and AGFG2) featured prominently among Class II diGly site proteins but were also found in other classes (SNX2 in Class I; YKT6, TRAPPC3, SNX3 in Class III; RAB35 in Class IV). Intriguingly, among Class III, we identified actin-linked proteins such as CNN2, ARPC3, ARPC5 and ARPC5L (**Figure 1H**). We verified LLOMe-induced ubiquitylation of CNN2 as well as of LAMP1, CD63, ARL8B, VAMP7, PICALM, and AGFG1 by Western blot following denaturing immunoprecipitation (**Figure S2A**). Moreover, we noted that CNN2, PICALM and AGFG1, which have not been directly linked to lysosomes, translocated from a peripheral distribution to the damaged lysosomes (**Figure S2B**) pointing to a direct involvement of the respective factors in lysophagy. Together, our detailed analysis identified a broad range of targets of lysosomal damage-induced ubiquitylation beyond mere constituents of the lysosome and including potential new regulators.

**CNN2 translocates to damaged lysosomes and is ubiquitylated for timely dissociation from lysosomes**

We selected CNN2 for further analysis because CNN2 had not been connected to autophagy or lysosomes. We confirmed translocation of endogenous CNN2 to Gal3-decorated damaged lysosomes by immunofluorescence in HeLa cells (**Figure 2A**), whereas we did not detect CNN2 on depolarized mitochondria or starvation-induced autophagosomes (data not shown). Lysophagy typically occurs within 6-12 h after damage (Maejima et al.,

2013). Intriguingly, CNN2 dissociated from the lysosomes within 2-3 h after damage before the damaged lysosomes were cleared as indicated by Gal3-positive vesicles remaining but lacking associated CNN2 (**Figure 2A, B**). Analysis of overexpressed CNN2-GFP confirmed timely dissociation of CNN2 from lysosomes (**Figure 2D, E**). To ask whether ubiquitylation played a role in CNN2 localization, we generated a CNN2-GFP 5xKR mutant with lysine-to-arginine substitutions at the 5 CNN2 ubiquitylation sites identified by our mass spectrometry approach (**Figure 2C**). The majority of these sites located in or near the CH domain. To prevent alternative ubiquitylation near these sites, we generated a second mutant, CNN2-GFP CH-KR, with all lysines in the CH domain substituted (**Figure 2C**). Both CNN2-GFP 5xKR and CNN2-GFP CH-KR readily translocated to damaged lysosomes like wild type CNN2-GFP (**Figure 2D, E and Figure S3A**). However, in contrast to wild type CNN2, both mutant proteins persisted on damaged lysosomes beyond 3 h (**Figure 2D, E and Figure S3A**), demonstrating that ubiquitylation at the right position of CNN2 is required for timely dissociation of CNN2 from, but not for localization to damages lysosomes. Western blot analysis showed that the overall ubiquitylation of CNN2 was not reduced by the 5xKR or the CH-KR mutations (**Figure S3B**), suggesting that ubiquitylation occurred at alternative sites in the mutant protein but that this ubiquitylation was not proficient for the particular mechanism of CNN2 dissociation. The role of ubiquitylation was confirmed by treatment with the ubiquitin E1 inhibitor MLN7243 that again led to persistence of CNN2 on lysosomes, whereas initial translocation of CNN2 to lysosomes was not affected (**Figure S3C, D**).

To exclude that involvement of CNN2 is restricted to chemical damage of a large fraction of cellular lysosomes, we used an approach that relies on optical generation of reactive oxygen species in order to trigger local damage to lysosomal membranes (Hung et al., 2013). In live cells, laser irradiation of photosensitizer-loaded lysosomes led to a rapid recruitment of Gal3 exclusively in the exposed area indicating spatially controlled lysosomal damage (**Figure 2F**). Importantly, CNN2-GFP translocated specifically to the damaged lysosomes and this localization increased for both the CH-KR and the 5xKR mutants (**Figure 2F and Figure S3E**) again showing that dynamic dissociation of CNN2 is regulated by ubiquitylation.

## CNN2 organizes actin filaments associated with damaged lysosomes for efficient lysophagy

Before further analyzing the significance of CNN2 ubiquitylation, we first aimed to address the role of CNN2 in lysophagy. Because CNN2 stabilizes actin filaments (Liu and Jin, 2016), we visualized actin in HeLa cells using the SPY650-FastAct probe that labels dynamic actin filaments (Lukinavicius et al., 2014). Using confocal super-resolution microscopy, we

detected actin associated with lysosomes specifically after lysosomal damage where it colocalized with Gal3 and CNN2 (**Figure 3A**) and LAMP1 (**Figure S4A and S4B**). FastAct also visualized stress fibers in optical sections closer to the bottom of the cell (**Figure S4C**). FastAct-labelled actin covered Gal3-positive damaged lysosomes, while CNN2 often formed a crescent on one side of the structure (**Figure 3A**). Actin association with lysosomes upon damage was also supported by extensive translocation of mCherry-tagged Arp5 to LAMP1-positive compartments (**Figure 3B and 3C**) in line with the identification of Arp2/3 subunits in our mass spectrometry screen (**Figure 1H**). Importantly, the FastAct signal on damaged lysosomes was significantly reduced in CNN2 HeLa knockout (KO) cells (**Figure 3D and 3E**) demonstrating that CNN2 helps organize actin filaments associated with damaged lysosomes.

We next asked whether CNN2 and its binding to actin was required for lysophagy. Autophagic clearance of damaged lysosomes can be assessed by following the number of Gal3-positive lysosomes over time in immunofluorescence microscopy (Aits et al., 2015). In control-depleted cells, Gal3-positive lysosomes were largely cleared over the course of 16 h, as expected (**Figure 3F-H**). In contrast, depletion of CNN2 with two independent siRNAs resulted in persistence of Gal3-positive lysosomes (**Figure 3F and S4D-F**) showing that damaged lysosomes were not efficiently cleared. The clearance defect was rescued by overexpression of wild type CNN2, but not of CNN2-ΔABS (**Figure 3F-H**) in which we deleted the actin binding sites (Liu and Jin, 2016), indicating that actin binding by CNN2 was essential for the function of CNN2 in lysophagy. Notably, while the CNN2-ΔABS mutant protein lost its binding to stress fibers, as expected, it still localized to damaged lysosomes (**Figure 3F**). We confirmed requirement of CNN2 (**Figure S4G-I**) and of actin-binding by CNN2 (see below in **Figure 6E and 6F**) for lysophagy in HeLa CNN2 KO cells. The translocation of Arp2/3 complex implied that Arp2/3-mediated actin branching on damaged lysosomes. Treatment with the Arp2/3 inhibitor CK-666 largely reduced the clearance of Gal3-decorated damaged lysosomes after LLOMe treatment (**Figure 3I and S4J**). Thus, both actin branching and CNN2-mediated actin stabilization are essential for efficient lysophagy.

**CNN2 is essential for autophagosome formation during lysophagy**

We next explored what step of lysophagy was regulated by CNN2. Recruitment of the autophagy receptor p62 (alias SQSTM1) to damaged lysosomes was not affected in CNN2-depleted versus control-depleted cells, and p62 even persisted for at least 16 h (**Figure 4A,**

**4B and S5A**) reflecting the observed clearance defect described above. In contrast to p62, recruitment of LC3 to damaged lysosomes was markedly impaired upon CNN2 depletion (**Figure 4C and 4D, and S5B**). This was determined by the percentage of Gal3-decorated lysosomes positive for LC3, but became particularly apparent by the reduction of LC3 rings around Gal3-decorated lysosomes in the CNN2-depleted cells (**Figure 4C**). We confirmed the requirement of CNN2 for LC3 recruitment in CNN2 KO cells (**Figure S5 C-D**) and showed that LC3 was rescued in CNN2 KO cells by expression of CNN2 wild type but not of the actin-binding deficient CNN2-ΔABS mutant protein (**Figure S5E and S5F**). Confocal super-resolution microscopy showed FastAct-labelled actin on Gal3-positive lysosomes inside the cavity of LC3-decorated phagophore and confirmed that LC3 was largely reduced on damaged lysosomes in CNN2 KO cells (**Figure 4E**) in line with the quantification above. We next asked whether the defect in phagophore formation correlated with a reduction of LC3-II formation by LC3 lipidation as detectable in Western blots. Whereas LC3 lipidation was stimulated by LLOMe-induced lysosome damage in wild type cells, as expected, this stimulation was reduced in CNN2 KO cells (**Figure 4F and G**). Chloroquine treatment confirmed that lower LC3-II levels in CNN2 KO cells were due to reduced lipidation rather than increased degradation (**Figure 4F and G**). The defect in lipidation also correlated with reduced degradation of TAX1BP1 (**Figure 4F and G**), consistent with TAX1BP1 being an autophagy receptor involved in lysophagy (Eapen et al., 2021). Thus, CNN2 is required for phagophore formation around damaged lysosomes during lysophagy.

**HSPB1 is associated with CNN2 and regulates lysophagy**

To gain further insight into function and regulation of CNN2 during lysophagy, we applied a proximity biotinylation approach in which a CNN2-APEX2 fusion protein was expressed in order to biotinylate proteins associated with CNN2 in either control or LLOMe-treated cells. Biotinylation was triggered by a pulse of $H_2O_2$ in the presence of biotin phenol. Biotinylated proteins were isolated by streptavidin in denaturing conditions and quantitatively compared by mass spectrometry (**Figure 5A and Table S2**). As expected, actin was detected in both conditions stressing the function of CNN2 in actin regulation (**Table S2**). Consistent with the observed translocation of CNN2 to lysosomes upon damage, we detected increased biotinylation of LGALS1 and LGALS3 (alias Gal1 and Gal3) after LLOMe treatment (**Figure 5A**). Of note, the small heat shock protein HSPB1 was found among the top hits after lysosomal damage (**Figure 5A**). We confirmed a stable interaction between CNN2 and HSPB1 and its stimulation by lysosome damage using co-immunoprecipitation (**Figure 5B**).

We further pursued HSPB1 because HSPB1 regulates actin and has previously been linked to autophagy (Vendredy et al., 2020). Moreover, mutation of HSPB1 is causative for late onset distal hereditary motor neuropathy and CMT disease, and HSPB1 may be neuroprotective in neuronal disease models (Vendredy et al., 2020). Immunofluorescence microscopy confirmed translocation of HSPB1 to Gal3-positive damaged lysosomes in HeLa cells where it colocalized with CNN2 (**Figure 5C-E)**. Depletion of CNN2 did not abolish HSPB1 recruitment to damaged lysosomes (data not shown) suggesting that HSPB1 has additional binding partners. Importantly, knockdown of HSPB1 by siRNA largely delayed the clearance of Gal3-positive damaged lysosomes in HeLa cells (**Figure 5F and S6A-B**), indicating a direct role of HSPB1 in lysophagy. Further analysis of progression of lysophagy in HSPB1-depleted cells revealed that damaged lysosomes failed to efficiently recruit LC3 **(Figure 5G, H and Figure S6C)**, which mirrored the effect of CNN2 depletion. Moreover, expression of HSPB1 with a dominant disease-associated S135F mutation in the alpha-crystallin domain largely impaired lysophagy compared to expression of HSPB1 wild type (**Figure 5I, J**) even though translocation of HSPB1 to damaged lysosomes was not affected by the mutation (**Figure S6D and S6E**), thus pointing to impaired lysophagy as a potential component of pathogenesis.

**p97 triggers timely removal of ubiquitylated CNN2 to promote lysophagy**

The effect of CNN2 or HSPB1 depletion on phagophore formation reflected the previously described consequence of inactivating the ubiquitin-targeting AAA ATPase p97 (Papadopoulos et al., 2017), pointing to a link between p97, CNN2 and HSPB1. In line with this notion, p97 colocalized with CNN2 on damaged lysosomes (**Figure S7A**). Importantly, time course analysis revealed that timely dissociation of CNN2 during lysophagy was largely impaired by pharmacological inhibition of p97 with NMS-873 (**Figure 6A, 6B and S7B**), suggesting that p97 extracts ubiquitylated CNN2 from damaged lysosomes.

Two hallmarks of p97-mediated regulation supported the notion that p97 targets CNN2 directly. First, inhibition of p97 during lysosomal damage led to an accumulation of polyubiquitylated CNN2 compared to CNN2 during lysosomal damage without p97 inhibition, as shown by denaturing immunoprecipitation of CNN2-GFP (**Figure 6C**). Second, in cells expressing variants of p97, CNN2 was strongly bound by the p97 substrate-trapping mutant E578Q but less so by wild-type p97, and this interaction was stimulated by LLOMe (**Figure 6D**). This contrasted with other regulators such as AGFG1 and PICALM that did not specifically bind p97-E578Q (**Figure S7C, D**), even though they were ubiquitylated during lysophagy (**Figure S2A**), thus demonstrating target selectivity by p97 in this process. In

general, p97-mediated extraction of ubiquitylated proteins from organelles or other structures is often followed by degradation in the proteasome. In line with that, proteasome inhibition led to persistence of CNN2 on damaged lysosomes (**Figure S7E and F**) suggesting that CNN2 was being degraded in a coupled p97- and proteasome-mediated reaction. We noted that also the cytosolic fraction of CNN2 was partially degraded following lysosome damage, which was reflected in a drop of total CNN2 levels (**Figure S7G**) and of cytosolic CNN2 staining (**Figure S7E**). This degradation was sensitive to proteasome inhibition but not to p97 inhibition (**Figure S7G**) supporting the notion that p97 specifically targets lysosome-associated CNN2 for subsequent degradation.

To further demonstrate that, specifically, CNN2 extraction from damaged lysosomes is required for lysophagy, we revisited our CNN2 ubiquitylation mutant CH-KR. Since CH-KR fails to be efficiently removed from damaged lysosome (**Figure 2D**), we inquired whether CH-KR impaired lysophagy. In CNN2 knockout cells, overexpression of wild type CNN2 rescued the defect in clearance of damaged lysosomes (**Figure 6E, F**). In contrast, the CNN2-CH-KR ubiquitylation mutant failed to fully rescue the clearance defect (**Figure 6E, F**). The defect was again at the level of phagophore formation, as shown by impaired LC3 recruitment that could be rescued by CNN2 wild type but not CH-KR (**Figure S8A, B**). These data concur that not only the function of CNN2 but also timely ubiquitylation and p97-triggered removal of CNN2 is essential for efficient phagophore formation and lysophagy. Because CNN2 recruitment does not require actin-binding (**Figure 3F**), we asked what CNN2 associates with on the damaged lysosomes. We again used CNN2 proximity biotinylation but now specifically asked which partners CNN2 stayed associated with when p97-mediated extraction was inhibited during a 2 h chase after LLOMe treatment. Quantitative mass spectrometry revealed several biotinylated targets including p62/SQSTM1 and p97/VCP that significantly increased upon p97 inhibition (**Figure S9A and Table S3**). Notably, CNN2 and p62 colocalized on damaged lysosomes while CNN2 recruitment was reduced upon depletion of p62 (**Figure S9B-D**) suggesting that p62 contributes to CNN2 recruitment and that p97 dissociates CNN2 from p62.

**HSPB1 cooperates with p97 in extracting CNN2**

In contrast to CNN2, we did not detect marked ubiquitylation of HSPB1 after lysosomal damage by Western blot (data not shown), suggesting that HSPB1 is not a target of p97 but rather a regulator that may cooperate with p97 in extracting CNN2. To explore this notion, we revisited the CNN2-APEX2 proximity approach with a simplified readout (Jia et al., 2020)

in which the proteins that are biotinylated by CNN2-APEX2 in different conditions were isolated and then compared by Western blot (**Figure 7A**). This approach confirmed the increase in HSPB1 association with CNN2 upon lysosomal damage observed by mass spectrometry (**Figure 5A**). Of note, concomitant inhibition of p97 by NMS-873 further increased association of HSBP1 with CNN2 and also led to trapping of p97 (**Figure 7A**). Importantly, depletion of HSPB1, like p97 inhibition, resulted in persistence of CNN2 on damaged lysosomes beyond 3 h (**Figure 7B, C**). Similarly, while LLOMe-treatment again increased CNN2 ubiquitylation, ubiquitylated CNN2 accumulated further upon HSPB1 depletion, and thus again mirrored the effect of p97 inhibition (**Figure 7D**). However, the combination of HSPB1 depletion and p97 inhibition did not further aggravate CNN2 persistence on damaged lysosomes (**Figure 7B, C**) and also did not further increase the accumulation of ubiquitylated CNN2 (**Figure 7D**), showing that effects of both treatments are not additive. Depletion of HSPB1 did not affect binding of p97-E578Q to CNN2 (**Figure S9E**) in co-immunoprecipitations consistent with HSPB1 being a small heat shock protein that stabilizes folding intermediates rather than a substrate adapter for p97. These data concur that HSPB1 and p97 cooperate, rather than working in parallel pathways, for the timely removal of ubiquitylated CNN2 from damaged lysosomes to promote lysophagy.

## Discussion

Ubiquitylation of lysosomal proteins is the defining modification that triages permeabilized lysosomes for clearance by lysophagy (Yim and Mizushima, 2020)·(Fujita et al., 2013). Here, we conducted systematic ubiquitin profiling of proteins tagged with ubiquitin during the lysosomal damage response. Our work uncovers the framework of how ubiquitin modification dictates the complex process of lysophagy through different layers of regulation.

Many of the identified targets are resident lysosomal proteins including LAMP1, TMEM192, CD63, PPT1, PPT2, GLA and TPP1 and these hits extend previous findings (Fujita et al., 2013; Yoshida et al., 2017). It is likely that the ubiquitylation of these proteins serves as “eat-me” signal to support engulfment by the phagophore by recruiting autophagy receptors (Eapen et al., 2021; Koerver et al., 2019; Maejima et al., 2013). Intriguingly, our analysis indicates that the ubiquitylation of resident proteins and autophagy factors such as LGALS1, LGALS3, SQSTM1 continues progressively during later stages of the damage response.

In contrast, we find that a first wave of ubiquitylation mainly targets membrane trafficking regulators thereby revealing a second layer of regulation. This includes SNAREs and SNARE regulators which likely illustrates the need to suppress fusion of damaged lysosomes with late endosomes or autophagosomes (Luzio et al., 2007). Consistent with that notion, ubiquitylation sites were identified in the functionally critical SNARE homology domains of VAMP8, VAMP7 and VAMP3 (Table S1). Moreover, we verified ubiquitylation and uncovered lysosome translocation of the SNARE adapters AGFG1 and PICALM that regulate VAMP7 and VAMP8, respectively, and that so far have rather been linked to endocytosis (Miller et al., 2007; Miller et al., 2011; Pryor et al., 2008). PICALM, which is associated with Alzheimer’s disease, has been connected to autophagy as it ensures SNARE delivery for the autophagic system (Harold et al., 2009; Moreau et al., 2014). The translocation of PICALM to damaged lysosomes shown here suggests an additional, more direct function of PICALM in lysophagy. Moreover, we identified ARL8B that not only controls lysosome fusion but also mediates transport of lysosomes to the cell periphery (Ballabio and Bonifacino, 2020). Lysosome positioning is regulated by ARL8B ubiquitylation at lysine-141 (Deshar et al., 2016), which was also found to be upregulated in this study. Therefore, ubiquitylation of ARL8B during lysophagy may suppress lysosomal fusion and favor transport of damaged lysosomes back to the cell center to facilitate engulfment by the phagophore.

In addition, our identification of the actin-stabilizing protein CNN2 and the Arp2/3 complex as targets of ubiquitylation uncovers a critical role of actin filaments during lysophagy. The fact that CNN2 depletion inhibits LC3 recruitment demonstrates a function specifically in phagophore formation in lysophagy. This concurs with the previous report that actin facilitates phagophore formation during starvation-induced macroautophagy (Mi et al., 2015), and suggests that a role of actin applies more generally also to selective macroautophagy. Importantly, by analyzing CNN2, we unravel a third layer of ubiquitin-mediated regulation that is governed by p97. We find that CNN2 exhibits a dynamic association with the damaged lysosome during the process of lysophagy and needs to be removed in a timely manner for lysophagy to occur (model in **Figure 7E**). This may reflect a need to transiently stabilize actin filaments, but then to release this stabilizing activity in order to allow formation of the phagophore, which is in line with the observed CNN2 dissociation before clearance of the damaged lysosome. Crucially, we demonstrate here that dynamic dissociation of CNN2 relies on CNN2 ubiquitylation at specific sites, as well as on the ubiquitin-directed segregase p97 and the proteasome. This is consistent with the general function of p97 in extracting ubiquitylated proteins from cellular structures based on its unfolding activity (Tanaka et al., 2010; van den Boom and Meyer, 2018; Ye et al., 2017) and reveals an interesting link of p97 to the actin cytoskeleton. Importantly, our finding uncovers a direct target of p97 in lysophagy and explains how p97 (with HSPB1) drives this process.

In addition, our work revealed a critical cooperation of p97 with HSPB1 during lysophagy. HSPB1 has already been connected to autophagy (Haidar et al., 2019; Tang et al., 2011) and shown to regulate the actin cytoskeleton (Dierick et al., 2005) which is in line with its link to CNN2 revealed in this study. In prokaryotes, small heat shock proteins are established partners of p97-related AAA ATPases that stabilize folding intermediates (Mogk et al., 2019). On the molecular level, it is therefore possible that HSPB1 transiently binds targets of p97 such as CNN2 to facilitate their unfolding and extraction by p97. Of note, p97 and HSPB1 are both associated with neurodegenerative diseases (Al-Obeidi et al., 2018; Vendredy et al., 2020), and disease-associated mutations in p97 affect lysosome homeostasis and lysophagy (Papadopoulos et al., 2017; Wall et al., 2021). The observation that also a HSPB1 disease mutant delays clearance of damaged lysosomes highlights impaired lysophagy as a possible component in neurodegeneration. While ubiquitylation targets in lysophagy have now been described, it will be important to further characterize and functionally unravel the ubiquitylation machinery in future studies to fully understand the pathway and its relevance for disease.

**Limitations of this study**

Due to the fact that our data were gathered and validated in a human cancer cell line, the implications of our findings for cellular homeostasis and signaling need to be tested for cell types and developmental stages of interest in organismal models.

**Acknowledgment:** We acknowledge the use of the imaging equipment and the support in microscope usage and image analysis by the Imaging Center Campus Essen (ICCE), Center of Medical Biotechnology (ZMB), University of Duisburg-Essen, and specifically thank N. Schulze and J. Koch for help. We thank C. Papadopoulos for generation of the CNN2 and CNN2ΔABS expression constructs. This work was supported by the Deutsche Forschungsgemeinschaft (DFG, German Research Foundation) project grant (Project-ID 447112704) to H.M. and C.B., by the Collaborative Research Center 1430 (Project-ID 424228829) to H.M, as well as by the Munich Cluster for Systems Neurology (EXC 2145 SyNergy – Project-ID 390857198) and the Collaborative Research Center 1177 (Project-ID 259130777) to C.B.

**Author contributions:** B.K. performed and analyzed the majority of cell-based experiments. P.G. helped with these experiments. T.B., A.S., S. L. and C.B. performed cell perturbations followed by MS, and MS data analysis. H.M. and C.B. conceived and supervised the project. H.M. wrote the manuscript.

**Competing interests:** The authors declare no competing interests.

**Main Figure legends:**

**Figure 1: Ubiquitin profiling of the lysosomal damage response**

**(A)** Triple SILAC diGly proteomics workflow. Cells were probed after mock-treatment (Light, L), directly after a 1 h LLOMe-treatment for the acute lysosome damage induction (Medium, M), and after a 2 h chase following LLOMe washout to reflect progression of the damage response (Heavy, H).
**(B)** diGly sites and ubiquitylated proteins across three triple SILAC experiments.
**(C)** Pearson's correlation coefficients of biological triplicates.
**(D)** LLOMe-induced ubiquitinome changes. Average intensities based on the summed extracted ion currents (XICs) of peptides carrying diGly sites are shown in relation to the fold change of regulation (log2 SILAC ratio). Top 20 increased and decreased diGly sites are marked. Sites highlighted in bold are shared in the two SILAC comparisons.
**(E)** Classification of regulated diGly sites (log2 (SILAC) ratio ≥1 in at least two data points) according to their increase over the 3 h time course.
**(F)** Annotation enrichment analysis of proteins with Class I, II, III and IV diGly sites from (e). The dot plot shows significantly overrepresented Uniport Sequence Feature (UP_SEQ) as well as gene ontology molecular functions (GO_MFs), cellular compartments (GO_CCs), and biological processes (GO_BPs).
**(G)** Frequency of diGly sites in proteins across the different diGly site classes.
**(H)** Heat map of log2 (SILAC) ratio for examples of proteins from different diGly site classes. *, Cav1_K39 and Cav1_K8 are identical site in in Cav1 isoforms 1 and 2, respectively.

**Figure 2: CNN2 translocates to damaged lysosomes and is ubiquitylated for timely dissociation**

**(A)** Dynamic association of endogenous CNN2 with damaged lysosomes in HeLa cells. Immunofluorescence of CNN2 and Gal3 as lysosomal damage marker after mock or LLOMe-treatment for indicated time periods. Note CNN2 translocation and dissociation before Gal3 clearance.
**(B)** Graph represents percentage of CNN2 and Gal3-positive vesicles among all Gal3-positive vesicles per cell. More than 30 cells were quantified per condition in each experiment (n=4 biologically independent experiments). One-way analysis of variance (ANOVA) with Tukey's multiple comparison test, **P=0.0036, ***P=0.0002 and ****P<0.0001. Error bars represent the mean ± s.e.m.

**(C)** Schematic domain structure of CNN2 with positions of identified ubiquitylation sites indicated. CH Domain, calponin homology domain; ABS1/2, actin binding sites.
**(D)** HeLa cells expressing CNN2-GFP wild type or harboring lysine-to-arginine substitutions in the CH domain (CH-KR) following mock or LLOMe treatment as indicated. Note that CNN2 wild type dissociates from LAMP1 vesicles within 3 h, but the ubiquitylation mutants persist. See Figure S3A for CNN2-GFP 5xKR covering the 5 ubiquitylation sites detected by MS.
**(E)** Quantification of D. Percentage of LAMP1 vesicles positive for CNN2. More than 20 cells were quantified. One-way ANOVA with Tukey's multiple comparison test, ***P=0.0003 and ****P<0.0001, ns – not significant. Error bars represent the mean ± s.d.
**(F)** Live cell imaging of HeLa cells expressing CNN2-GFP CH-KR and mCherry-Gal3. Lysosomes were loaded with photosensitizer AIPcS2a, irradiated in the indicated area and chased over the course of 1 h. See Figure S3E for wild type and CNN2 5xKR imaging data.
**(A), (D), (F),** Scale bars, 10 µm.

**Figure 3: CNN2 links actin regulation to lysophagy**

**(A)** Actin filaments are recruited along with CNN2 to damaged lysosomes. HeLa cells were stained with live cell actin probe FastAct 1 h prior to indicated treatments and then fixed for additional immunostaining of CNN2 and the damage marker Gal3. Images were taken and processed by super-resolution confocal microscopy.
**(B)** The Arp2/3 complex translocates to damaged lysosomes. Stable cells expressing mCh-Arp5 were fixed after mock or LLOMe-treatment, stained with LAMP1 antibody.
**(C)** Quantification of (B). Percentage of LAMP1 vesicles positive for mCh-Arp5. More than 40 cells were quantified. Error bar represents the mean ± s.d.
**(D)** Actin association with damaged lysosomes is reduced in CNN2 KO cells (clone #3). Cells were mock or LLOMe treated as indicated. Actin was visualized by FastAct and Gal3 by immunostaining. See Figure S4I for KO verification.
**(E)** Quantification of D. Mean Intensity of FastAct localized to Gal3 vesicles was measured and presented on the graph. Approximately two thousand FastAct-Gal3 double positive vesicles from more than 30 cells were analyzed in each experiment (n=3 biologically independent experiments). Unpaired t test, ***P=0.0003. Error bars represent the mean ± s.e.m.
**(F)** Actin-binding by CNN2 is essential for lysophagy. Depletion-rescue experiments. Control HeLa cells or HeLa cells expressing siRNA-resistant CNN2-GFP wild type (wt) or CNN2-GFP lacking the actin-binding sites (ΔABS) as indicated were treated with CNN2 siRNA#2

(see Figure S4F for depletion efficiency) and clearance of Gal3-decorated damaged lysosomes was monitored after LLOMe washout. Note that expression of siRNA-resistant CNN2 wild type, but not of CNN2 ΔABS, rescued the clearance of damaged lysosomes after CNN2 depletion. See Figure S4D, E for effect of siRNA#1 and Figure S4G, H for clearance defect confirmed in CNN2 KO cells.
**(G)** Quantification of F. Gal3 clearance assay. Cells with >3 Gal3 vesicles were scored and shown as percentage of all quantified cells. >30 cells were quantified per condition in each experiment (n=3 biologically independent experiments). Two-way ANOVA with Tukey's multiple comparison test, ****P<0.0001, ns – not significant. Error bars represent the mean ± s.e.m.
**(H)** Western blot verification of CNN2 depletion and CNN2-GFP expression.
(**I**) Inhibition of the Arp2/3 complex by CK-666 impairs lysophagy. Gal3 clearance assay. Quantification was performed as in (G). 1 h LLOMe treatment followed by indicated chase times in the presence of CK-666 or vehicle alone. See Figure S4J for respective imaging data.
**(A)** Scale bar 5 µm. **(B), (D), (F),** Scale bars, 10 µm.

**Figure 4: CNN2 is essential for autophagosome formation during lysophagy**

**(A)** CNN2 depletion does not impair p62 recruitment but leads to accumulation of p62-decorated damaged lysosomes. Control and CNN2-depleted cells were mock or LLOMe-treated, or treated and chased as indicated. Immunofluorescence of Gal3 and p62. See Figure S5A for siCNN2#2 imaging data and split channels.
**(B)** Quantification of (A). Cells with >3 p62 and Gal3 double positive vesicles were scored and presented as the percentage of total number of cells. >30 cells were quantified per condition in each experiment (n=3 biologically independent experiments). Two-way ANOVA with Tukey's multiple comparison test, ****P<0.0001. Error bars represent the mean ± s.e.m.
**(C)** CNN2 depletion inhibits LC3 recruitment. Immunofluorescence with antibodies specific for MAP1LC3 isoforms A, B, C (LC3) and Gal3 in control or CNN2-depleted cells. Note reduced formation of LC3-rings around Gal3-positive vesicles. See Figure S5B for siCNN2#2 and mock treatments, Figure S5C,D for confirmation in CNN2 KO cells, and Figure S5E,F showing requirement of actin-binding by CNN2 for LC3 recruitment.
**(D)** Quantification of (C). Graph shows percentage of LC3 and Gal3 double positive vesicles among all Gal3 vesicles per cell. More than 30 cells were quantified per condition in each experiment (n=3 biologically independent experiments). Two-way (ANOVA) with Sidak's multiple comparison test, ****P<0.0001. Error bars represent the mean ± s.e.m.

**(E)** Super-resolution confocal microscopy of LC3 and actin on Gal3-labelled damaged lysosomes in parental and CNN2 KO cells. Cells were treated with FastAct dye prior to indicated LLOMe treatment, and stained with LC3 and Gal3 antibodies. Note that actin and Gal3-labelled lysosomes are found within the cavity of LC3-decorated phagophores in parental cells, while actin and LC3 recruitment is markedly reduced in CNN2 KO cells.
**(F)** Lysosome damage-induced LC3 lipidation is impaired in CNN2 KO cells. Parental and CNN2 KO cells were treated as indicated and lysates analyzed by Western blot with antibodies to LC3, TAX1BP1, CNN2 and tubulin. Note that the lipidated LC3-II is reduced in CNN2 KO cells, and that reduction is due to reduced lipidation and not by increased autophagy flux as shown by chloroquine (CQ) treatment.
**(G)** Quantification of the normalized LC3-II and TAX1BP1 signal in (F). LC3 II (n=3 independent experiments) or TAX1BP1 (n=2) band intensities were quantified and normalized to Tubulin. Two-way (ANOVA) with Sidak's multiple comparison test, **P=0.0089 (-CQ) or 0.0029 (+CQ), *P=0.0324. Error bars, mean ± s.d.
**(A), (C),** Scale bars, 10 µm. **(E),** Scale bar 5 µm or 1 µm (inset).

**Figure 5: HSPB1 associates with CNN2 and is required for lysophagy**

**(A)** Proximity biotinylation identifies HSPB1 as CNN2 partner after lysosome damage. SILAC-labelled stable CNN2-APEX2 expressing cells were mock (light-labeled, L) or LLOMe (heavy-labeled, H) treated and pulsed with biotin phenol (30 min) and $H_2O_2$ (1 min). Biotinylated proteins were quantitatively compared by mass spectrometry and data depicted as volcano plot. Red and blue dots denote significantly enriched or reduced proteins, respectively. Proteins in bold are discussed in the text.
**(B)** Co-immunoprecipitation of CNN2 with HSPB1 and its stimulation by lysosome damage. Treatments as indicated in HSPB1-myc, and GFP or CNN2-GFP expressing cells. Pulldowns with GFP nanobodies.
**(C)** Colocalization of HSPB1 and CNN2 on damaged lysosomes. Immunofluorescence of endogenous CNN2 and HSPB1 in GFP-Gal3 expressing HeLa cells.
**(D)** Quantification of HSPB1 localization on Gal3 decorated damaged lysosomes and colocalizing HSPB1 and CNN2 on lysosomes in (C). The graph represents percentage of HSPB1 and Gal3 double positive vesicles divided by the total number of Gal3 vesicles per cell. More than 30 cells were quantified per condition in each experiment (n=2 biologically independent experiments). Unpaired Student's t-test, *P=0.0258.
**(E)** Quantification of colocalisation of CNN2 on HSPB1-positive vesicles. >30 cells are quantified per condition. Error bar represents the mean ± s.d.

**(F)** HSPB1 is required for lysophagic flux. Gal3 clearance assay after LLOMe-induced damage in control or HSPB1 depleted cells as indicated. Quantification as described in Figure 3G. Two-way ANOVA with Tukey's multiple comparison test, ****P<0.0001. See Figure S6A for imaging data and S6B for depletion verification.
**(G)** Impaired phagophore formation in HSPB1-depleted HeLa cells. LC3 and Gal3 immunofluorescence 2 h after LLOMe washout. Note reduced formation of LC3-rings around Gal3-positive vesicles. See Figure S6C for siHSPB1#2 data and mock treatments.
**(H)** Quantification of G. Graph represents percentage of LC3 and Gal3-positive vesicles of all Gal3 vesicles per cell. >30 cells were quantified per condition in each experiment (n=3 biologically independent experiments). Two-way (ANOVA) with Sidak's multiple comparison test, *P=0.0292.
**(I)** Disease-associated HSBP1-S135F mutant impairs clearance of damaged lysosomes. LLOMe-treatment in HeLa cell lines stably expressing HSPB1 wild type (wt) or HSPB1 S135F mutant protein. Note that Gal3-positive damaged lysosomes persist in the HSPB1-S135F mutant cell line after 16 h chase. See Figure S6D, E showing equal recruitment of HSPB1-S135F and HSPB1 wt proteins.
**(J)** Quantification of (I) as described in Figure 3G. n=3 biological independent experiments. Two-way ANOVA with Sidak's multiple comparison test, ***P=0.0005.
**(D), (F), (H), (J**) Error bars represent the mean ± s.e.m.
**(C), (G), (I)** Scale bars, 10 µm.

**Figure 6: p97 removes ubiquitylated CNN2 from damaged lysosomes for lysophagy**

**(A)** p97 is required for timely dissociation of CNN2 to facilitate lysophagy. HeLa cells were treated with LLOMe in the presence of p97 inhibitor NMS-873 or vehicle alone, and stained for endogenous CNN2 and Gal3. Note CNN2 persistence on Gal3 vesicles specifically upon p97 inhibition. See Figure S7B for single channel Gal3 images and S7A for colocalization of p97 and CNN2.
**(B)** Quantification of A. Graph represents percentage of CNN2 and Gal3-positive vesicles among all Gal3 vesicles per cell. >30 cells were quantified per condition in each experiment (n=2 biologically independent experiments). One-way analysis of variance (ANOVA) with Sidak's multiple comparison test, *P=0.0396, ns – not significant. Error bars represent the mean ± s.e.m.
**(C)** Ubiquitylated CNN2 accumulates upon p97 inhibition in LLOMe-treated cells. Cells expressing CNN2-GFP protein were LLOMe-treated and chased for two hours in the presence or absence of NMS-873 prior to lysis. CNN2-GFP was isolated under denaturing conditions using GFP-nanobodies and ubiquitylation analyzed by Western blot.

**(D)** CNN2 is bound specifically by the p97-E578Q substrate-trapping mutant after LLOMe-induced lysosome damage. CNN2-GFP co-immunoprecipitation from stable cell lines after expression of p97 wild type or p97-E578Q and 2 h LLOMe treatment followed by Western blot.
**(E)** Persistent CNN2 CH-KR impairs lysophagy. CNN2 knockout or parental HeLa cells were transfected with GFP alone, or with CNN2-GFP wild type or the CNN2-GFP CH-KR ubiquitylation site mutant, or the CNN2 ΔABS mutant for comparison, as indicated. Cells were LLOMe-treated, washed and chased for 16 h and the number of Gal3-positive damaged lysosomes determined. Note that the clearance defect in CNN2 knockout cells was rescued by expression of CNN2 wild type, but not of CNN2 CH-KR (or CNN2-ΔABS as negative control). Magnified insets showing the persistence of CNN2 CH-KR but not of CNN2-ΔABS on Gal3-positive damaged lysosomes. See Figure S8A, B for defect of CNN2 CH-KR in rescuing LC3 recruitment.
**(F)** Quantification of (E). Cells with >5 Gal3 vesicles were scored and presented as the percentage of total number of cells. More than 20 cells were quantified per condition in each experiment (n=3 biologically independent experiments). Note, only transfected cells were analyzed. Two-way ANOVA with Tukey's multiple comparison test, **P= 0.0021, ***P=0.0001, ****P<0.0001, ns – not significant. Error bars represent the mean ± s.e.m.
**(A), (E)** Scale bars, 10 μm.

**Figure 7: p97 and HSPB1 cooperate in removing ubiquitylated CNN2 from lysosomes**

**(A)** HSPB1 is trapped on CNN2 in the absence of p97 activity. Proximity biotinylation analyzed by Western blot in indicated conditions of lysosome damage (LLOMe) and p97 inhibition (NMS-873). Cells expressing CNN2-APEX2 were treated with LLOMe for 1 h and chased for 2 h after washout prior to addition of $H_2O_2$ to trigger biotinylation.
**(B)** Loss of p97 or HSPB1 function impairs CNN2 dissociation in a non-additive manner. Time course of CNN2 localization to damaged lysosomes upon p97 inhibition (NMS-873), HSPB1 depletion or a combination of both as indicated. Scale bar, 10 μm.
**(C)** Quantification of B. Graph represents percentage of CNN2 and Gal3-positive vesicles among all Gal3-positive vesicles per cell. More than 30 cells were quantified per condition in each experiment (n=3 biologically independent experiments). Two-way ANOVA with Tukey's multiple comparison test, ****P<0.0001; ***P=0.0004; *P=0.0118. Error bars represent the mean ± s.e.m.
**(D)** HSPB1 acts downstream of ubiquitylation together with p97. HeLa cells stably expressing CNN2-GFP were LLOMe-treated for 1 h and chased for 2 h prior to denaturing lysis upon indicated treatments after p97 inhibition (NMS-873), HSPB1 siRNA or a

combination of both as indicated. Ubiquitylation of CNN2 was assessed by Western blot after immunoprecipitation using GFP nanobodies. Note that loss of HSPB1, or p97 inhibition, leads to increased accumulation of ubiquitylated CNN2 after LLOMe-induced damage, but that effects are not additive.

**(E)** Model. After lysosome damage, various resident proteins become ubiquitylated to serve as anchor point for autophagy receptor-mediated recruitment the LC3-decorated phagophore. CNN2 is recruited by associating with the p62 autophagy receptor and then stabilizes actin filaments that assist phagophore formation. CNN2 needs to be subsequently ubiquitylated and removed by p97 with the help of HSPB1 to allow efficient phagophore formation.

## STAR METHODS

## RESOURCE AVAILABILITY

### Lead contact

Further information and requests for resources and reagents should be directed to and will be fulfilled by Hemmo Meyer (*hemmo.meyer@uni-due.de*).

### Materials availability

Plasmids and cell lines generated in this study will be available upon request.

### Data and code availability

- Original Western blot data and microscopy images used in this paper have been deposited at Mendeley Data and are publicly available as of the date of publication. The DOIs are listed in the key resources table.
- The mass spectrometry proteomics data have been deposited to the ProteomeXchange Consortium via the PRIDE partner repository (https://www.ebi.ac.uk/pride/archive/) with the dataset identifiers PXD029926 and PXD032903.
- Any additional information required to reanalyze the data reported in this paper is available from the lead contact upon request.

## EXPERIMENTAL MODEL AND SUBJECT DETAILS

### Cell lines

HeLa cells (Kyoto) or Hek293T cells were cultured in Dulbecco's modified Eagle's medium (DMEM) supplemented with 10% fetal bovine serum (FBS, PAN-Biotech) and 1% Penicillin/Streptomycin (PAN-Biotech). Cells were grown in standard conditions, 37°C and 5% $CO_2$. HeLa stable cell lines were cultured in DMEM supplemented with 10% FCS, 1% Penicillin/Streptomycin and 500 µg/ml G418 as selection antibiotic. For generation of stable cell lines (CNN2-GFP, HSPB1 wt or S135F-myc, mCherry-Arp5 and GFP-Gal3), HeLa Kyoto cells were transfected with circular pEGFP N1 CNN2, pcDNA3 HSPB1 wt or S135F-myc, pmCherry C1-Arp5 or pEGFP-hGal3 plasmids, respectively and selected in DMEM containing 10% FBS, 1% Penicillin/Streptomycin and selection antibiotic G418 (600 µg/ml for 3 days and 900 µg/ml for 10 days). HeLa cells stably expressing CNN2-myc-APEX2 were obtained by lentiviral transduction followed by selection with antibiotics. Briefly, for virus generation, 1 µg of pMD2.G and 1µg of pPAX2 retroviral packaging plasmid were transfected into Hek293T

cells together with 1 µg of pHAGE-C-myc-APEX2 CNN2. Target HeLa cells were transduced with virus containing medium, which was exchanged to growth medium after 24 h. Transduced cells were selected with 2 µg/ml Puromycin (Sigma). HeLa CNN2 KO cells were generated using Calponin 2 Double Nickase Plasmid (Santa Cruz Biotechnology, sc-402882-NIC) according to manufacturer's instructions. Cell lines were not authenticated.

## METHOD DETAILS

### Reagents and cell treatments

To induce lysosomal damage, HeLa cells were treated with 1 mM L-Leucyl-L-Leucine methyl ester hydrobromide (LLOMe, Sigma) for 1 h (unless otherwise stated) and chased for indicated times. For CNN2 dissociation assays, HeLa cells were treated with 50 µM MLN7243 (TAK-243, CT-M7243-5, Hoelzel Diagnostics) or 5 µM NMS-873 (SML1128, Sigma Aldrich) for 15 min prior to addition of LLOMe, and throughout the chase. For CNN2 protein degradation assay from the whole cell lysate, HeLa cells were treated with 5 µM NMS-873 or 20 µM MG132 (Calbiochem, 474790) as described above. For Arp2/3 inhibition, cells were treated with 100 nM CK-666 (SML0006, Sigma Aldrich) for indicated times. Chloroquine was used at 100 µM.

To visualize actin filaments, HeLa cells were treated with SPY650-FastAct™ (Spirochrome) according to manufacturer's instructions. Briefly, SPY650-FastAct™ was added to the cells 1 h prior to addition of LLOMe and was incubated on cells throughout the LLOMe treatment and/or chase.

### Plasmids

IMAGE clone 8860204 (Source Bioscience) was used as template for the amplification of human CNN2 open reading frame (ORF) with primers containing XhoI (5'-CACACTCGAGATGAGCTCCACGCAGTTCAAC-3') or HindIII (5'-CTGCGAAGCTTGTAGCCGGCCTCCTCCTG-3') restriction sites and subcloned into pEGFP N1 (Clontech). CNN2 lysine-to-arginine mutants 5xKR (K19, K30, K52, K134, K234 mutated) and CH-KR (all lysines in the CH domain (amino acid residues 13-132) were mutated to arginines) were ordered as g-block DNA fragments (Integrated DNA Technologies) containing XhoI and HindIII (NEB) restriction sites and subcloned into pEGFP N1 vector. pEGFP N1 CNN2 ΔABS (ABS-actin binding sites) plasmid, lacking amino acid residues 146-190, was generated by site-directed mutagenesis using following oligos (5'-TATGACCCCAAGAACCATATC-3' and 5'- CTTGACGCCAATGTCCAC-3'). pHAGE-C-myc-APEX2 CNN2 plasmid was generated from pDONR223-CNN2 (without stop codon) as donor

vector (Horizon Discovery) by recombination-based cloning using the Gateway system (Invitrogen).

Human HSPB1 coding sequence (codon optimized) was ordered as a g-block (Integrated DNA Technologies) containing HindIII and BamHI restriction sites and subcloned into pcDNA3.1 vector to get a C-terminal myc-tagged fusion protein. Human HSPB1 S135F disease mutant was generated by site directed mutagenesis using the following oligos (5'-GGCTATATCTTCAGATGCTTTACAAG-3' and 5'-ATGCTCATCTTGTCGTTCTTCG-3'). To generate pmCherry C1-ArpC5 plasmid, ArpC5 ORF was amplified from complementary DNA (generated from RNA isolated from HeLa cells by RT reaction) using the following oligos containing EcoRI (5'-CTCGAATTCCATGTCGAAGAACACAGTG-3') and BamHI (5'-CTCGGATCCCTACACAGTTTTTCTTGC-3') restriction sites and subcloned into pmCherry C1 (Clontech). To generate pcDNA5 FRT/TO GFP-AGFG1 plasmid, AGFG1 ORF was amplified from complementary DNA using following oligos containing attB sites (5'-GGGGACCAAGTTTGTACAAAAAAGCAGGCTTCATGGCGGCCAGCGCGAAGC-3' and 5'-GGGGACCACTTTGTACAAGAAAGCTGGGTCCTATAAGAAAGGATTGGTT-3') and subcloned into pDONR221 vector (Invitrogen) and then into pcDNA5 FRT/TO GFP vector (described before (Hulsmann et al., 2018)) using the Gateway cloning system. Human PICALM was subcloned from pmCherry C1 PICALM (previously generated by B.K. by restriction cloning using HeLa cDNA as a template for PICALM ORF amplification) into pEGFP C1 (Clontech) by restriction cloning using XhoI and BamHI restriction enzymes (NEB).

The following plasmids were ordered from Addgene: pEGFP-hGal3 (#73080) (Maejima et al., 2013), Arp3-pmCherry C1 (#27682) (Taylor et al., 2011), pEGFP VAMP7 (#42316) (Martinez-Arca et al., 2000), pEGFP C2-CD63 was a kind gift from Paul Luzio (#62964), pDEST47-Arl8B-GFP was a gift from Richard Kahn (#67404). LAMP1–GFP was a kind gift from J. Gruenberg (University of Geneva, Switzerland). mCherry C1-Gal3 and p97 plasmids were described before (Koerver et al., 2019)(Ritz et al., 2011).

Plasmid DNA was transfected using Lipofectamine 2000 (Thermo Fisher Scientific) according to manufacturer's instructions 24 h prior to experiments.

**RNA isolation and reverse transcription**

Total RNA was isolated from HeLa cells using TRIzol reagent (Invitrogen) according to manufacturer's instructions. Complementary DNA (cDNA) was synthetized from 4 µg RNA using SuperScript™ II Reverse Transcriptase (Invitrogen) according to manufacturer's instructions.

**siRNA knockdown**

To deplete human CNN2, HSPB1 and p62, the siRNAs listed in the key resources table were used. The siRNAs (final concentration 10 nM) were transfected into HeLa cells using Lipofectamine RNAi Max according to manufacturer's instructions (Thermo Fisher Scientific) 48 or 72 hours prior to analysis. Depletion efficiency was verified by Western blot.

**Cell lysis and co-immunoprecipitation**

HeLa cells were rinsed twice with ice-cold PBS and lysed in lysis buffer (150 mM KCl, 50 mM Tris pH 7.4, 5 mM $MgCl_2$, 5% Glycerol, 1% Triton X-100, 2 mM β-mercaptoethanol) supplemented with protease (complete EDTA-free protease inhibitor cocktail, Roche) and phosphatase inhibitors (PhosStop, Roche). The soluble fractions were obtained after centrifugation at 17000g for 5 min and directly used for SDS PAGE and western blotting or for subsequent co-immunoprecipitation experiments. For co-immunoprecipitation, cell lysates were incubated with GFP nanobody-coupled Sepharose beads for 1 h with constant rotation at 4°C. Beads were washed 3x with ice-cold lysis buffer containing inhibitors. Proteins were eluted with Laemmli buffer, boiled at 95°C for 5 min and analyzed by Western blotting. To detect ubiquitylation of biotinylated proteins, cells expressing indicated tagged proteins were denatured in TSD buffer (50 mM Tris-HCL, pH 7.5, 1% SDS, and 5 mM DTT), then diluted with TNN buffer (20 mM Tris-HCl, pH 7.5, 200 mM NaCl, 0.5% NP-40, and protease inhibitor cocktail) (Tanaka et al., 2010). To detect ubiquitylation of biotinylated proteins, cleared lysates were incubated with GFP-coupled Sepharose beads or with Streptavidin Sepharose High Performance beads (GE Healthcare), respectively as described above. Beads were washed 3x with ice-cold TNN buffer containing 0.2% SDS and further processed as described above prior to use for SDS PAGE and Western blotting.

**Western blotting**

Samples were resolved by SDS PAGE and transferred to nitrocellulose membrane (Amersham, GE Healthcare). The membranes were blocked in 3% BSA in PBST (PBS containing 0.05% Tween 20) for 1 h at room temperature (RT). Primary antibodies listed in the key resources table were diluted in 3% BSA in PBST or 5% milk in PBST and incubated overnight at 4°C or 2 h at RT. The membranes were washed 3x in PBST and incubated with secondary antibodies listed in the key resources table (diluted 1:10000 in 5% milk in PBST) for 1 h at RT. Signals were visualized with SuperSignal West Pico Chemiluminescent substrate (Pierce) or ECL Prime Western Blotting Detection Reagent (Amersham).

**Immunofluorescence staining and confocal microscopy**

Cells were cultured on coverslips, fixed in 4% paraformaldehyde, permeabilized with 0.1% Triton X-100 in PBS for 10 min at RT and blocked with 3% bovine serum albumin in PBS with 0.1% Triton X-100 and 0.1% saponin for 1 h at RT. Primary and secondary antibodies listed in the key resources table were diluted in blocking solution and incubated on cells for 1 h at RT. Indirect immunofluorescence staining was followed by mounting in ProLong Gold (Thermo Fisher Scientific). Confocal laser scanning microscopy was performed on a TCS SP5 AOBS (Leica Microsystems) system equipped with standard PMT detectors as well as sensitive HyD detectors, a 63×/1.4 NA oil immersion objective or an HC PL APO 20×/0.7NA dry objective. Lasers used were HeNe 633 nm, DPSS 561 nm, Ar 488 nm and Diode 405 nm. Acquisition and hardware were controlled by LAS AF software (Leica Microsystems).
Images were processed using Fiji software (https://imagej.net/Fiji), Adobe Photoshop, and Illustrator. Automated quantifications were done with Cell Profiler software 44. Graphs and statistical analysis were prepared using Excel (Microsoft Corporation) or GraphPad Prism 9.0 (GraphPad Software).

**Confocal super-resolution microscopy**

High resolution images were acquired on Leica TCS SP8X Falcon confocal microscope (Leica Microsystems), equipped with HyDs SMD detectors, HC PL APO 63x/1.4 Oil CS2 objective and the Leica Application Suite X (LAS-X) software version 3.5.7 with the LAS X Lightning Expert module. Confocal image stacks of damaged lysosomes were captured separately in sequential scans (4x zoom, scan speed 478 Hz), using white light (WLL) and 405 nm diode lasers. For Z-stack imaging, the confocal pinhole was set to 0.63 AU, and the Z-step size was system optimized (0.13 µm). Approximately 25-30 Z stacks were taken per cell. Pictures were deconvolved with the Leica Lightning module using ‘’Adaptive’’ strategy based on the refractive index (1.44) of the Prolonged Gold mounting medium.

**Live cell microscopy and photodamage**

Live cell imaging was performed at 37°C in imaging medium (P04-03591, PAN-Biotech) supplemented with 10% FCS and L-Glutamine (11500626, Fisher Scientific). Confocal spinning disk microscopy with laser induced lysosomal damage used in Figure 2 was performed on an Eclipse Ti-E (Nikon) inverted microscope with an Andor AOTF Laser Combiner, a CSU-X1 Yokogawa spinning disk unit and an iXon3 897 single photon detection EMCCD camera (Andor Technology). Laser lines used for excitation of EGFP and RFP were 488 nm and 561 nm, respectively. Images were acquired using a CFI Apo TIRF 60x/1.49 or CFI APO TIRF 100×/1.49NA oil-immersion objectives (Nikon). To induce LMP with light, cells were treated with 125 nM AlPcS2a (P40632, Frontier Scientific) as described before (Hung et

al., 2013). LMP was induced with a 640 nm laser through defined regions in HeLa cells for 4 x 1 ms using Andor Revolution FRAP and Photo Activation illumination system (FRAPPA). Image acquisition was controlled by Andor IQ3 Software (Andor Technology).

**DiGly proteomics**

HeLa cells were cultured in lysine- and arginine-free DMEM supplemented with dialyzed FBS, 2 mM L-glutamine, 1 mM sodium pyruvate, penicillin/streptomycin and light (K0) lysine (38 µg/mL) and arginine (66 µg/ml). Medium and heavy media were the same except the light lysine was replaced with K4 (L-Lysine, 2HCl 4.4.5.5-D4, Cambridge Isotope Laboratories Inc.) and K8-lysine (L-Lysine, 2HCl U-13C U-15N, Cambridge Isotope Laboratories Inc), respectively. Medium and heavy labeled cells were treated for 1 h with 250 µM LLOMe (Sigma) while light labelled were treated for 1 h with vehicle alone (EtOH). Light and heavy cells were repeatedly washed with fresh SILAC medium and cultured without LLOMe for another 2 h. Cells were processed as described before (Fiskin et al., 2016). Briefly, cells were washed twice with ice-cold PBS and lysed in 5 ml denaturing lysis buffer (8 M Urea, 50 mM Tris pH 8, 50 mM NaCl, 1X PIC (protease inhibitor cocktail, EDTA-free, Roche), 50 µM DUB inhibitor PR-619 (Millipore)). Samples were incubated on ice for 10 min and then sonicated with 3x 20 s pulses. Following removal of non-solubilized material (15,000xg/10 min), differentially labelled lysates were mixed at equal ratios based on total protein determined by BCA (Pierce-Thermo; typically 25-35 mg of total protein). Following reduction with 5 mM DTT and alkylation with 10 mM chloroacetamide, lysates were digested with 5 ng/µl lys-C (Wako) for 1 h at room temperature. Subsequent digestion of peptides with trypsin (Promega) was performed as described (Villen and Gygi, 2008). Lyophilized peptides were resuspended in 1.5 ml IAP buffer (50 mM MOPS pH 7.4, 10 mM $Na_2HPO_4$, 50 mM NaCl) and centrifuged to remove any insoluble material (2500xg/5 min). The supernatant was incubated with anti-diGly antibody (32 µg/IP) conjugated to protein A agarose beads (Cell Signaling) for 1 h at 4°C. Unbound peptides were removed through 3x washing with IAP buffer and once with PBS. Bound material was eluted 4x with 50 µl 0.15% TFA and peptides were desalted using C18 stage-tip method (Rappsilber et al., 2003). Each sample was immunoprecipitated sequentially three times and each IP was analyzed separately by mass spectrometry. Peptides samples were separated on a nanoflow HPLC system (Thermo Scientific) using a 226 min gradient of 5-33% acetonitrile containing 0.5% acetic acid on custom filled C18 reversed-phase columns and analyzed on a hybrid ion-trap Orbitrap mass spectrometer (Orbitrap Elite, Thermo Scientific) using data-dependent acquisition selecting the most intense peaks from each full MS scan acquired in the Orbitrap for subsequent MS/MS while excluding peptides with unassigned charge states or charge states below +3 from fragmentation (see RAW files for specific settings). Raw data files from triplicate samples were processed with MaxQuant (1.6.0.1) as

described previously (Cox and Mann, 2008; Cox et al., 2011) using a human (UP000005640) UNIPROT database and the following parameter settings: first search peptide mass tolerance 20 ppm, main search peptide mass tolerance 0.5 Da, tryptic digestion allowing up to two missed cleavages, cysteine carbamidomethylation (57.021464) as fixed modification, methionine oxidation (15.994946), N-terminal protein acetylation (42.010565) and diGG (114.042927; excluded from C-terminus) as variable modifications, revert decoy mode and peptide, protein and site FDR ≤ 0.01. Perseus (1.6.5.0) was used for data sorting. diGly sites were considered regulated, if they showed >2-fold change. Functional annotation enrichment analysis was performed using DAVID (Huang et al., 2007) coupled to significance determination using Fisher's exact test and correction for multiple hypothesis testing by the Benjamini and Hochberg FDR. Heat maps were generated using MultiExperiment Viewer (Saeed et al., 2003).

**Proximity proteomics**

HeLa cells stably expressing CNN2-APEX2 were grown in lysine- and arginine-free DMEM supplemented with FBS, L-Glutamine, Sodium pyruvate, heavy arginine (R10) (38 µg/ml) and lysine (K8) (66 µg/ml) or light arginine (R0) (38 µg/ml) and lysine (K0) (66 µg/ml), respectively. Heavy-labelled cells were treated with 250 µM LLOMe (Sigma) for 3 h at 37°C, while light-labelled cells were treated with vehicle alone (EtOH). Proximity labeling was performed essentially as described before (Korver et al., 2019). Briefly, cells were incubated with 500 µM Biotin-Phenol during the last 30 min of LLOMe treatment and subsequently pulsed by addition of $H_2O_2$ for 1 min at room temperature. To stop the biotinylation reaction, they were washed 3x with quencher solution (10 mM sodium azide, 10 mM sodium ascorbate, 5 mM Trolox in DPBS) and 3x with PBS. All further steps were performed at 4°C unless indicated otherwise. After cell harvest with 0.25% Trypsin/EDTA (Thermo Fisher Scientific), cells were counted and heavy- and light-labelled cells were mixed at a 1:1 ratio based on total cell numbers. After centrifugation, the resulting cell pellets were lysed in APEX-RIPA (50 mM Tris, 150 mM NaCl, 0.1% SDS, 1% Triton X-100, 0.5% sodium deoxycholate supplemented with 10 mM sodium ascorbate, 1 mM sodium azide, 1 mM Trolox and protease inhibitors (Roche Complete)). Samples were sonicated 2x for 1 s, spun down at 10,000xg for 10 min before application to streptavidin agarose resin (Thermo Fisher Scientific) and incubation with overhead shaking overnight. Subsequently, samples were washed 3x in APEX-RIPA buffer and 3x in 3 M Urea buffer (in 50 mM ABC) followed by incubation with TCEP (5 mM final) for 30 min at 55°C with shaking. After alkylation with IAA (10 mM final) for 20 min at room temperature in the dark the reaction was quenched with DTT (20 mM final). Samples were washed 2x with 2 M Urea (in 50 mM ABC) before trypsin digestion overnight at 37°C (20 µg/ml final). The resin was spun down and supernatants containing digested peptides were collected. After washing the resin

2x with 2 M Urea and pooling all supernatants the samples were acidified with TFA (1% final). Digested peptides were desalted on custom-made C18 stage tips (Rappsilber et al., 2003). Using an Easy-nLC1200 liquid chromatography (Thermo Fisher Scientific), peptides were loaded onto custom filled C18 reversed-phase columns and separated using a gradient of 5%–33% acetonitrile in 0.5% acetic acid over 90 min and detected on an Q Exactive HF mass spectrometer (Thermo Fisher Scientific). Dynamic exclusion was enabled for 30 s and singly charged species or species for which a charge could not be assigned were rejected. MS data was processed and analyzed using MaxQuant (1.6.0.1) (Cox and Mann, 2008; Cox et al., 2011) and Perseus (1.6.5.0). All proximity experiments were performed in quintuplicates. Unique and razor peptides were used for quantification. Matches to common contaminants, reverse identifications and identifications based only on site-specific modifications were removed prior to further analysis. Log2 H/L ratios were calculated. A threshold based on a log2 fold change of ≥ 1-fold or ≤ -1 was chosen so as to focus the data analysis on a small set of proteins with the largest alterations in abundance.

**QUANTIFICATION AND STATISTYCAL ANALYSIS**

All quantitative data are presented as the mean ± s.e.m. or ± s.d. of biologically independent samples, unless stated otherwise. Statistical analysis was carried out using GraphPad Prism 9.0 software. One- or two-way ANOVA was used to determine statistical significance. Student t-tests were used to determine statistical significance between treatments for proximity proteomics experiment or where ANOVA analysis was not applicable due to the experimental setup. A p-value <0.05 was considered statistically significant.

**Table S1: Quantitative ubiquitin remnant mass spectrometry data comparing control and LLOMe treated cells, related to Figure 1.**

**Table S2: CNN2 proximity biotinylation mass spectrometry data comparing control and LLOMe treated cells, related to Figure 5.**

**Table S3: CNN2 proximity biotinylation mass spectrometry data comparing LLOMe-treated cells with LLOMe and NMS873-treated cells, related to Figure Figures 6 and S9**

**References**


Aits, S., Kricker, J., Liu, B., Ellegaard, A.M., Hamalisto, S., Tvingsholm, S., Corcelle-Termeau, E., Hogh, S., Farkas, T., Holm Jonassen, A.*, et al.* (2015). Sensitive detection of lysosomal membrane permeabilization by lysosomal galectin puncta assay. Autophagy *11*, 1408-1424.

Al-Obeidi, E., Al-Tahan, S., Surampalli, A., Goyal, N., Wang, A.K., Hermann, A., Omizo, M., Smith, C., Mozaffar, T., and Kimonis, V. (2018). Genotype-phenotype study in patients with valosin-containing protein mutations associated with multisystem proteinopathy. Clin Genet *93*, 119-125.

Arhzaouy, K., Papadopoulos, C., Schulze, N., Pittman, S.K., Meyer, H., and Weihl, C.C. (2019). VCP maintains lysosomal homeostasis and TFEB activity in differentiated skeletal muscle. Autophagy, 1082-1099.

Ballabio, A., and Bonifacino, J.S. (2020). Lysosomes as dynamic regulators of cell and organismal homeostasis. Nat Rev Mol Cell Biol *21*, 101-118.

Chauhan, S., Kumar, S., Jain, A., Ponpuak, M., Mudd, M.H., Kimura, T., Choi, S.W., Peters, R., Mandell, M., Bruun, J.A.*, et al.* (2016). TRIMs and Galectins Globally Cooperate and TRIM16 and Galectin-3 Co-direct Autophagy in Endomembrane Damage Homeostasis. Dev Cell *39*, 13-27.

Cox, J., and Mann, M. (2008). MaxQuant enables high peptide identification rates, individualized p.p.b.-range mass accuracies and proteome-wide protein quantification. Nat Biotechnol *26*, 1367-1372.

Cox, J., Neuhauser, N., Michalski, A., Scheltema, R.A., Olsen, J.V., and Mann, M. (2011). Andromeda: a peptide search engine integrated into the MaxQuant environment. J Proteome Res *10*, 1794-1805.

Deshar, R., Moon, S., Yoo, W., Cho, E.B., Yoon, S.K., and Yoon, J.B. (2016). RNF167 targets Arl8B for degradation to regulate lysosome positioning and endocytic trafficking. The FEBS journal *283*, 4583-4599.

Dierick, I., Irobi, J., De Jonghe, P., and Timmerman, V. (2005). Small heat shock proteins in inherited peripheral neuropathies. Ann Med *37*, 413-422.

Eapen, V.V., Swarup, S., Hoyer, M.J., Paulo, J.A., and Harper, W. (2021). Quantitative proteomics reveals the selectivity of ubiquitin-binding autophagy receptors in the turnover of damaged lysosomes by lysophagy. eLife *10*, e72328.

Fiskin, E., Bionda, T., Dikic, I., and Behrends, C. (2016). Global Analysis of Host and Bacterial Ubiquitinome in Response to Salmonella Typhimurium Infection. Mol Cell *62*, 967-981.

Fujita, N., Morita, E., Itoh, T., Tanaka, A., Nakaoka, M., Osada, Y., Umemoto, T., Saitoh, T., Nakatogawa, H., Kobayashi, S.*, et al.* (2013). Recruitment of the autophagic machinery to endosomes during infection is mediated by ubiquitin. J Cell Biol *203*, 115-128.

Gabande-Rodriguez, E., Perez-Canamas, A., Soto-Huelin, B., Mitroi, D.N., Sanchez-Redondo, S., Martinez-Saez, E., Venero, C., Peinado, H., and Ledesma, M.D. (2019). Lipid-induced lysosomal damage after demyelination corrupts microglia protective function in lysosomal storage disorders. EMBO J *38*, e99553.

Gomez-Sintes, R., Ledesma, M.D., and Boya, P. (2016). Lysosomal cell death mechanisms in aging. Ageing research reviews *32*, 150-168.

Haidar, M., Asselbergh, B., Adriaenssens, E., De Winter, V., Timmermans, J.P., Auer-Grumbach, M., Juneja, M., and Timmerman, V. (2019). Neuropathy-causing mutations in HSPB1 impair autophagy by disturbing the formation of SQSTM1/p62 bodies. Autophagy *15*, 1051-1068.

Harold, D., Abraham, R., Hollingworth, P., Sims, R., Gerrish, A., Hamshere, M.L., Pahwa, J.S., Moskvina, V., Dowzell, K., Williams, A.*, et al.* (2009). Genome-wide association study identifies variants at CLU and PICALM associated with Alzheimer's disease. Nat Genet *41*, 1088-1093.

Huang, D.W., Sherman, B.T., Tan, Q., Kir, J., Liu, D., Bryant, D., Guo, Y., Stephens, R., Baseler, M.W., Lane, H.C.*, et al.* (2007). DAVID Bioinformatics Resources: expanded annotation database and novel algorithms to better extract biology from large gene lists. Nucleic Acids Res *35*, W169-175.

Hulsmann, J., Kravic, B., Weith, M., Gstaiger, M., Aebersold, R., Collins, B.C., and Meyer, H. (2018). AP-SWATH Reveals Direct Involvement of VCP/p97 in Integrated Stress Response Signaling Through Facilitating CReP/PPP1R15B Degradation. Mol Cell Proteomics *17*, 1295-1307.

Hung, Y.H., Chen, L.M., Yang, J.Y., and Yang, W.Y. (2013). Spatiotemporally controlled induction of autophagy-mediated lysosome turnover. Nature communications *4*, 2111.

Jia, J., Abudu, Y.P., Claude-Taupin, A., Gu, Y., Kumar, S., Choi, S.W., Peters, R., Mudd, M.H., Allers, L., Salemi, M.*, et al.* (2018). Galectins Control mTOR in Response to Endomembrane Damage. Mol Cell *70*, 120-135 e128.

Jia, J., Bissa, B., Brecht, L., Allers, L., Choi, S.W., Gu, Y., Zbinden, M., Burge, M.R., Timmins, G., Hallows, K.*, et al.* (2020). AMPK, a Regulator of Metabolism and Autophagy, Is Activated by Lysosomal Damage via a Novel Galectin-Directed Ubiquitin Signal Transduction System. Mol Cell *77*, 951-969 e959.

Koerver, L., Papadopoulos, C., Liu, B., Kravic, B., Rota, G., Brecht, L., Veenendaal, T., Polajnar, M., Bluemke, A., Ehrmann, M.*, et al.* (2019). The ubiquitin-conjugating enzyme UBE2QL1 coordinates lysophagy in response to endolysosomal damage. EMBO Rep *20*, e48014.

Liu, E.A., Schultz, M.L., Mochida, C., Chung, C., Paulson, H.L., and Lieberman, A.P. (2020). Fbxo2 mediates clearance of damaged lysosomes and modifies neurodegeneration in the Niemann-Pick C brain. JCI Insight *5*, e136676.

Liu, R., and Jin, J.P. (2016). Calponin isoforms CNN1, CNN2 and CNN3: Regulators for actin cytoskeleton functions in smooth muscle and non-muscle cells. Gene *585*, 143-153.

Logan, T., Simon, M.J., Rana, A., Cherf, G.M., Srivastava, A., Davis, S.S., Low, R.L.Y., Chiu, C.L., Fang, M., Huang, F.*, et al.* (2021). Rescue of a lysosomal storage disorder caused by Grn loss of function with a brain penetrant progranulin biologic. Cell *184*, 4651-4668 e4625.

Lukinavicius, G., Reymond, L., D'Este, E., Masharina, A., Gottfert, F., Ta, H., Guther, A., Fournier, M., Rizzo, S., Waldmann, H.*, et al.* (2014). Fluorogenic probes for live-cell imaging of the cytoskeleton. Nat Methods *11*, 731-733.

Luzio, J.P., Pryor, P.R., and Bright, N.A. (2007). Lysosomes: fusion and function. Nat Rev Mol Cell Biol *8*, 622-632.

Maejima, I., Takahashi, A., Omori, H., Kimura, T., Takabatake, Y., Saitoh, T., Yamamoto, A., Hamasaki, M., Noda, T., Isaka, Y.*, et al.* (2013). Autophagy sequesters damaged lysosomes to control lysosomal biogenesis and kidney injury. EMBO J *32*, 2336-2347.

Martinez-Arca, S., Alberts, P., Zahraoui, A., Louvard, D., and Galli, T. (2000). Role of tetanus neurotoxin insensitive vesicle-associated membrane protein (TI-VAMP) in vesicular transport mediating neurite outgrowth. J Cell Biol *149*, 889-900.

Mi, N., Chen, Y., Wang, S., Chen, M., Zhao, M., Yang, G., Ma, M., Su, Q., Luo, S., Shi, J.*, et al.* (2015). CapZ regulates autophagosomal membrane shaping by promoting actin assembly inside the isolation membrane. Nat Cell Biol *17*, 1112-1123.

Miller, S.E., Collins, B.M., McCoy, A.J., Robinson, M.S., and Owen, D.J. (2007). A SNARE-adaptor interaction is a new mode of cargo recognition in clathrin-coated vesicles. Nature *450*, 570-574.

Miller, S.E., Sahlender, D.A., Graham, S.C., Honing, S., Robinson, M.S., Peden, A.A., and Owen, D.J. (2011). The molecular basis for the endocytosis of small R-SNAREs by the clathrin adaptor CALM. Cell *147*, 1118-1131.

Mogk, A., Ruger-Herreros, C., and Bukau, B. (2019). Cellular Functions and Mechanisms of Action of Small Heat Shock Proteins. Annu Rev Microbiol *73*, 89-110.

Moreau, K., Fleming, A., Imarisio, S., Lopez Ramirez, A., Mercer, J.L., Jimenez-Sanchez, M., Bento, C.F., Puri, C., Zavodszky, E., Siddiqi, F.*, et al.* (2014). PICALM modulates autophagy activity and tau accumulation. Nature communications *5*, 4998.

Nakamura, S., Shigeyama, S., Minami, S., Shima, T., Akayama, S., Matsuda, T., Esposito, A., Napolitano, G., Kuma, A., Namba-Hamano, T.*, et al.* (2020). LC3 lipidation is essential for TFEB activation during the lysosomal damage response to kidney injury. Nat Cell Biol *22*, 1252-1263.

Papadopoulos, C., Kirchner, P., Bug, M., Grum, D., Koerver, L., Schulze, N., Poehler, R., Dressler, A., Fengler, S., Arhzaouy, K.*, et al.* (2017). VCP/p97 cooperates with YOD1, UBXD1 and PLAA to drive clearance of ruptured lysosomes by autophagy. EMBO J *36*, 135-150.

Papadopoulos, C., Kravic, B., and Meyer, H. (2020). Repair or Lysophagy: Dealing with Damaged Lysosomes. J Mol Biol *432*, 231-239.

Pryor, P.R., Jackson, L., Gray, S.R., Edeling, M.A., Thompson, A., Sanderson, C.M., Evans, P.R., Owen, D.J., and Luzio, J.P. (2008). Molecular basis for the sorting of the SNARE VAMP7 into endocytic clathrin-coated vesicles by the ArfGAP Hrb. Cell *134*, 817-827.

Radulovic, M., Schink, K.O., Wenzel, E.M., Nahse, V., Bongiovanni, A., Lafont, F., and Stenmark, H. (2018). ESCRT-mediated lysosome repair precedes lysophagy and promotes cell survival. EMBO J *37*, e99753.

Rappsilber, J., Ishihama, Y., and Mann, M. (2003). Stop and go extraction tips for matrix-assisted laser desorption/ionization, nanoelectrospray, and LC/MS sample pretreatment in proteomics. Anal Chem *75*, 663-670.

Ritz, D., Vuk, M., Kirchner, P., Bug, M., Schütz, S., Hayer, A., Bremer, S., Lusk, C., Baloh, R.H., Lee, H.*, et al.* (2011). Endolysosomal sorting of ubiquitinated caveolin-1 is regulated by VCP/p97 and UBXD1 and impaired by VCP disease mutations. Nat Cell Biol *13*, 1116-1123.

Saeed, A.I., Sharov, V., White, J., Li, J., Liang, W., Bhagabati, N., Braisted, J., Klapa, M., Currier, T., Thiagarajan, M.*, et al.* (2003). TM4: a free, open-source system for microarray data management and analysis. Biotechniques *34*, 374-378.

Skowyra, M.L., Schlesinger, P.H., Naismith, T.V., and Hanson, P.I. (2018). Triggered recruitment of ESCRT machinery promotes endolysosomal repair. Science *360*, eaar5078.

Tanaka, A., Cleland, M.M., Xu, S., Narendra, D.P., Suen, D.F., Karbowski, M., and Youle, R.J. (2010). Proteasome and p97 mediate mitophagy and degradation of mitofusins induced by Parkin. J Cell Biol *191*, 1367-1380.

Tang, D., Kang, R., Livesey, K.M., Kroemer, G., Billiar, T.R., Van Houten, B., Zeh, H.J., 3rd, and Lotze, M.T. (2011). High-mobility group box 1 is essential for mitochondrial quality control. Cell Metab *13*, 701-711.

Taylor, M.J., Perrais, D., and Merrifield, C.J. (2011). A high precision survey of the molecular dynamics of mammalian clathrin-mediated endocytosis. PLoS Biol *9*, e1000604.

Thiele, D.L., and Lipsky, P.E. (1990). Mechanism of L-leucyl-L-leucine methyl ester-mediated killing of cytotoxic lymphocytes: dependence on a lysosomal thiol protease, dipeptidyl peptidase I, that is enriched in these cells. Proc Natl Acad Sci U S A *87*, 83-87.

van den Boom, J., and Meyer, H. (2018). VCP/p97-Mediated Unfolding as a Principle in Protein Homeostasis and Signaling. Mol Cell *69*, 182-194.

Vendredy, L., Adriaenssens, E., and Timmerman, V. (2020). Small heat shock proteins in neurodegenerative diseases. Cell Stress Chaperones *25*, 679-699.

Villen, J., and Gygi, S.P. (2008). The SCX/IMAC enrichment approach for global phosphorylation analysis by mass spectrometry. Nature protocols *3*, 1630-1638.

Wall, J.M., Basu, A., Zunica, E.R.M., Dubuisson, O.S., Pergola, K., Broussard, J.P., Kirwan, J.P., Axelrod, C.L., and Johnson, A.E. (2021). CRISPR/Cas9-engineered Drosophila knock-in models to study VCP diseases. Dis Model Mech *14*, dmm048603.

Watts, G.D., Wymer, J., Kovach, M.J., Mehta, S.G., Mumm, S., Darvish, D., Pestronk, A., Whyte, M.P., and Kimonis, V.E. (2004). Inclusion body myopathy associated with Paget disease of bone and frontotemporal dementia is caused by mutant valosin-containing protein. Nat Genet, 377-381.

Ye, Y., Tang, W.K., Zhang, T., and Xia, D. (2017). A Mighty "Protein Extractor" of the Cell: Structure and Function of the p97/CDC48 ATPase. Frontiers in molecular biosciences *4*, 39.

Yim, W.W., and Mizushima, N. (2020). Lysosome biology in autophagy. Cell Discov *6*, 6.

Yoshida, Y., Yasuda, S., Fujita, T., Hamasaki, M., Murakami, A., Kawawaki, J., Iwai, K., Saeki, Y., Yoshimori, T., Matsuda, N.*, et al.* (2017). Ubiquitination of exposed glycoproteins by SCFFBXO27 directs damaged lysosomes for autophagy. Proc Natl Acad Sci U S A *114*, 8574-8579.

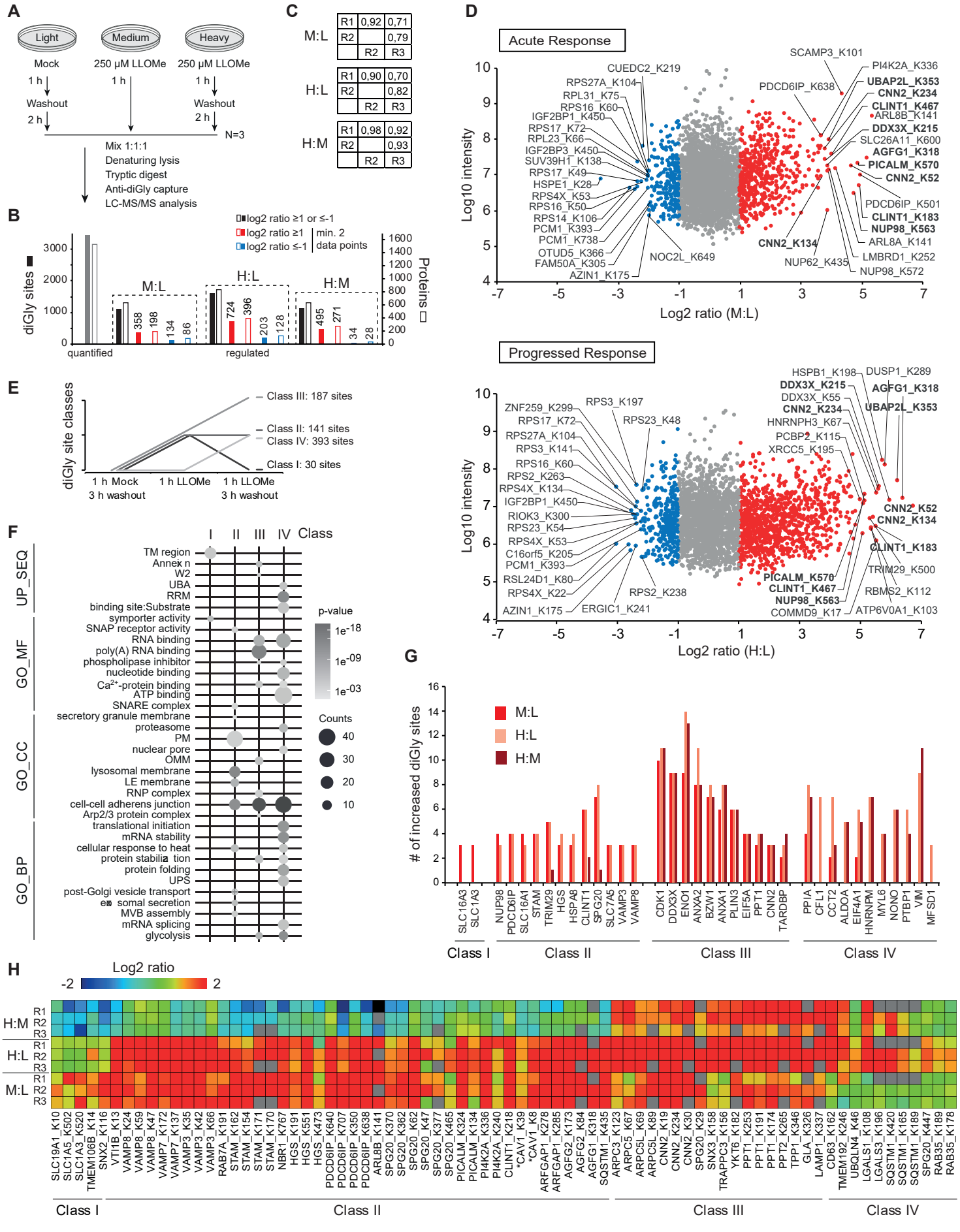
A
Light
Medium
Heavy
Mock
250 µM LLOMe
250 µM LLOMe
1 h
Washout
2 h
N=3
Mix 1:1:1
Denaturing lysis
Tryptic digest
Anti-diGly capture
LC-MS/MS analysis
B
log2 ratio ≥1 or ≤-1
log2 ratio ≥1
log2 ratio ≤-1
min. 2 data points
diGly sites
Proteins
M:L
H:L
H:M
358
198
134
86
724
396
203
128
495
271
34
28
quantified
regulated
C
M:L
H:L
H:M
R1 0,92 0,71
R2 0,79
R2 R3
R1 0,90 0,70
R2 0,82
R2 R3
R1 0,98 0,92
R2 0,93
R2 R3
D
Acute Response
Log10 intensity
Log2 ratio (M:L)
CUEDC2_K219
RPS27A_K104
RPL31_K75
RPS16_K60
IGF2BP1_K450
RPS17_K72
RPL23_K66
IGF2BP3_K450
SUV39H1_K138
RPS17_K49
HSPE1_K28
RPS4X_K53
RPS16_K50
RPS14_K106
PCM1_K393
PCM1_K738
OTUD5_K366
FAM50A_K305
AZIN1_K175
NOC2L_K649
SCAMP3_K101
PDCD6IP_K638
PI4K2A_K336
UBAP2L_K353
CNN2_K234
CLINT1_K467
ARL8B_K141
DDX3X_K215
SLC26A11_K600
AGFG1_K318
PICALM_K570
CNN2_K52
PDCD6IP_K501
CLINT1_K183
NUP98_K563
ARL8A_K141
LMBRD1_K252
NUP98_K572
CNN2_K134
NUP62_K435
Progressed Response
Log10 intensity
Log2 ratio (H:L)
ZNF259_K299
RPS3_K197
RPS17_K72
RPS23_K48
RPS27A_K104
RPS3_K141
RPS16_K60
RPS2_K263
RPS4X_K134
IGF2BP1_K450
RIOK3_K300
RPS23_K54
RPS4X_K53
C16orf5_K205
PCM1_K393
RSL24D1_K80
RPS4X_K22
AZIN1_K175
ERGIC1_K241
RPS2_K238
HSPB1_K198
DUSP1_K289
DDX3X_K215
AGFG1_K318
DDX3X_K55
CNN2_K234
UBAP2L_K353
HNRNPH3_K67
PCBP2_K115
XRCC5_K195
CNN2_K52
CNN2_K134
CLINT1_K183
TRIM29_K500
PICALM_K570
CLINT1_K467
NUP98_K563
RBMS2_K112
COMMD9_K17
ATP6V0A1_K103
E
diGly site classes
Class III: 187 sites
Class II: 141 sites
Class IV: 393 sites
Class I: 30 sites
1 h Mock
3 h washout
1 h LLOMe
3 h washout
1 h LLOMe
3 h washout
F
Class
I
II
III
IV
UP_SEQ
GO_MF
GO_CC
GO_BP
TM region
Annexin
W2
UBA
RRM
binding site:Substrate
symporter activity
SNAP receptor activity
RNA binding
poly(A) RNA binding
phospholipase inhibitor
nucleotide binding
Ca2+-protein binding
ATP binding
SNARE complex
secretory granule membrane
proteasome
PM
nuclear pore
OMM
lysosomal membrane
LE membrane
RNP complex
cell-cell adherens junction
Arp2/3 protein complex
translational initiation
mRNA stability
cellular response to heat
protein stabilization
protein folding
UPS
post-Golgi vesicle transport
exosomal secretion
MVB assembly
mRNA splicing
glycolysis
p-value
1e-18
1e-09
1e-03
Counts
40
30
20
10
G
# of increased diGly sites
M:L
H:L
H:M
SLC16A3
SLC1A3
NUP98
PDCD6IP
SLC16A1
STAM
TRIM29
HGS
HSPA8
CLINT1
SPG20
SLC7A5
VAMP3
VAMP8
CDK1
DDX3X
ENO1
ANXA2
BZW1
ANXA1
PLIN3
EIF5A
PPT1
CNN2
TARDBP
PPIA
CFL1
CCT2
ALDOA
EIF4A1
HNRNPM
MYL6
NONO
PTBP1
VIM
MFSD1
Class I
Class II
Class III
Class IV
H
Log2 ratio
-2
2
H:M
H:L
M:L
R1
R2
R3
SLC19A1_K10
SLC1A5_K502
SLC1A3_K520
TMEM106B_K14
SNX2_K116
VTI1B_K13
VAMP8_K24
VAMP8_K59
VAMP8_K47
VAMP7_K172
VAMP7_K137
VAMP3_K35
VAMP3_K42
VAMP3_K66
RAB7A_K191
STAM_K162
STAM_K154
STAM_K171
STAM_K170
NBR1_K767
HGS_K191
HGS_K551
HGS_K473
PDCD6IP_K640
PDCD6IP_K707
PDCD6IP_K350
PDCD6IP_K638
ARL8B_K141
SPG20_K370
SPG20_K362
SPG20_K62
SPG20_K47
SPG20_K377
SPG20_K465
PICALM_K324
PICALM_K134
PI4K2A_K336
PI4K2A_K240
CLINT1_K218
*CAV1_K39
*CAV1_K8
ARFGAP1_K278
ARFGAP1_K285
AGFG2_K173
AGFG2_K84
AGFG1_K318
SQSTM1_K435
ARPC3_K123
ARPC5_K67
ARPC5L_K69
ARPC5L_K89
CNN2_K19
CNN2_K234
CNN2_K30
SPG20_K29
SNX3_K158
TRAPPC3_K156
YKT6_K182
PPT1_K253
PPT1_K191
PPT1_K174
PPT2_K265
TPP1_K346
GLA_K326
LAMP1_K337
CD63_K162
TMEM192_K246
UBQLN4_K46
LGALS1_K108
LGALS3_K196
LGALS3_K420
SQSTM1_K165
SQSTM1_K189
SPG20_K447
RAB35_K189
RAB35_K178
Class I
Class II
Class III
Class IV

**Figure 1**

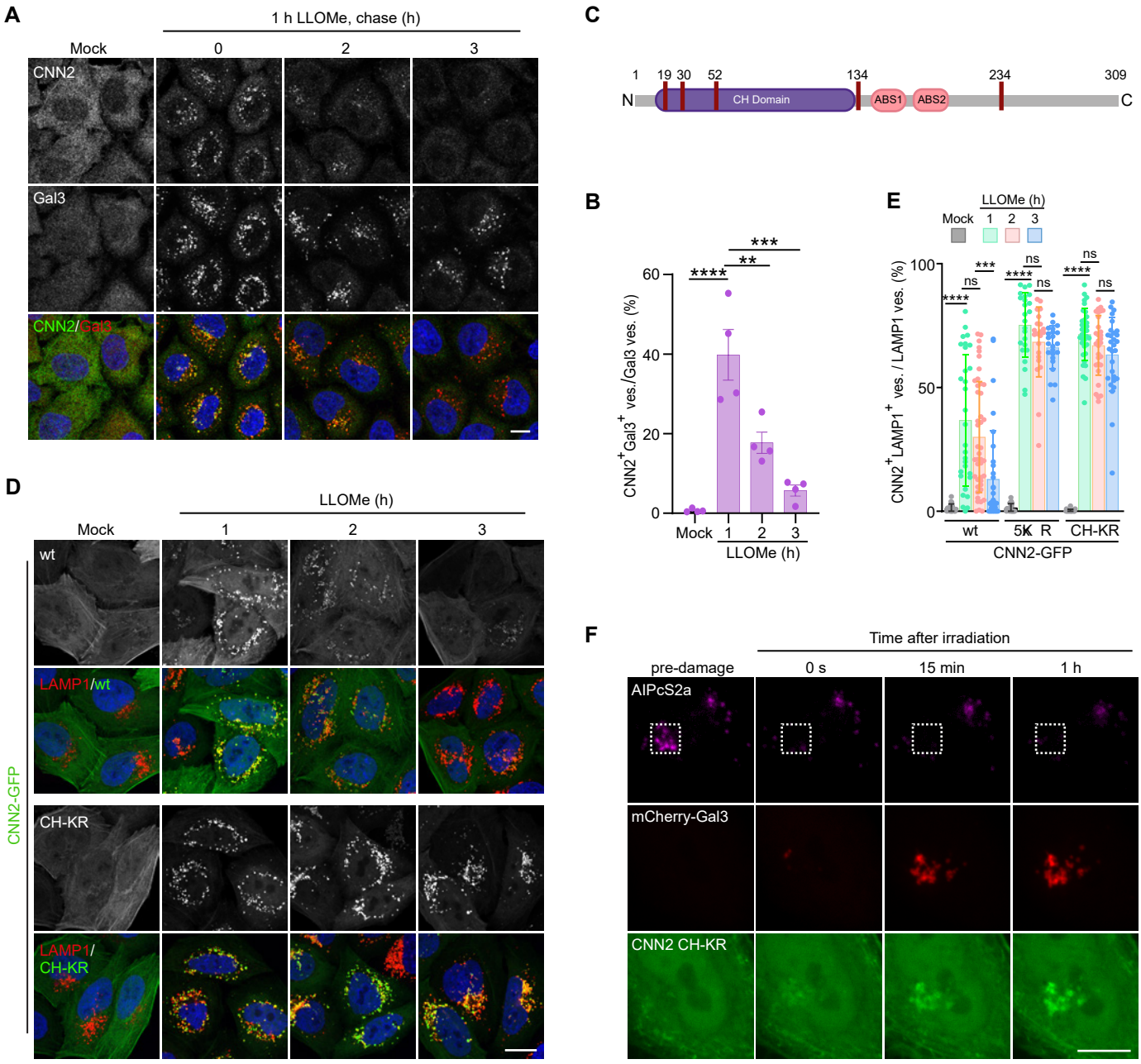
A
1 h LLOMe, chase (h)
Mock
0
2
3
CNN2
Gal3
CNN2/Gal3
C
1
19
30
52
134
234
309
N
CH Domain
ABS1
ABS2
C
B
***
**
****
60
40
20
0
CNN2+Gal3+ ves./Gal3 ves. (%)
Mock
1
2
3
LLOMe (h)
E
LLOMe (h)
Mock
1
2
3
100
50
0
CNN2+LAMP1+ ves. / LAMP1 ves. (%)
***
****
ns
wt
5K R
CH-KR
CNN2-GFP
D
LLOMe (h)
Mock
1
2
3
CNN2-GFP
wt
LAMP1/wt
CH-KR
LAMP1/
CH-KR
F
Time after irradiation
pre-damage
0 s
15 min
1 h
AIPcS2a
mCherry-Gal3
CNN2 CH-KR

**Figure 2**

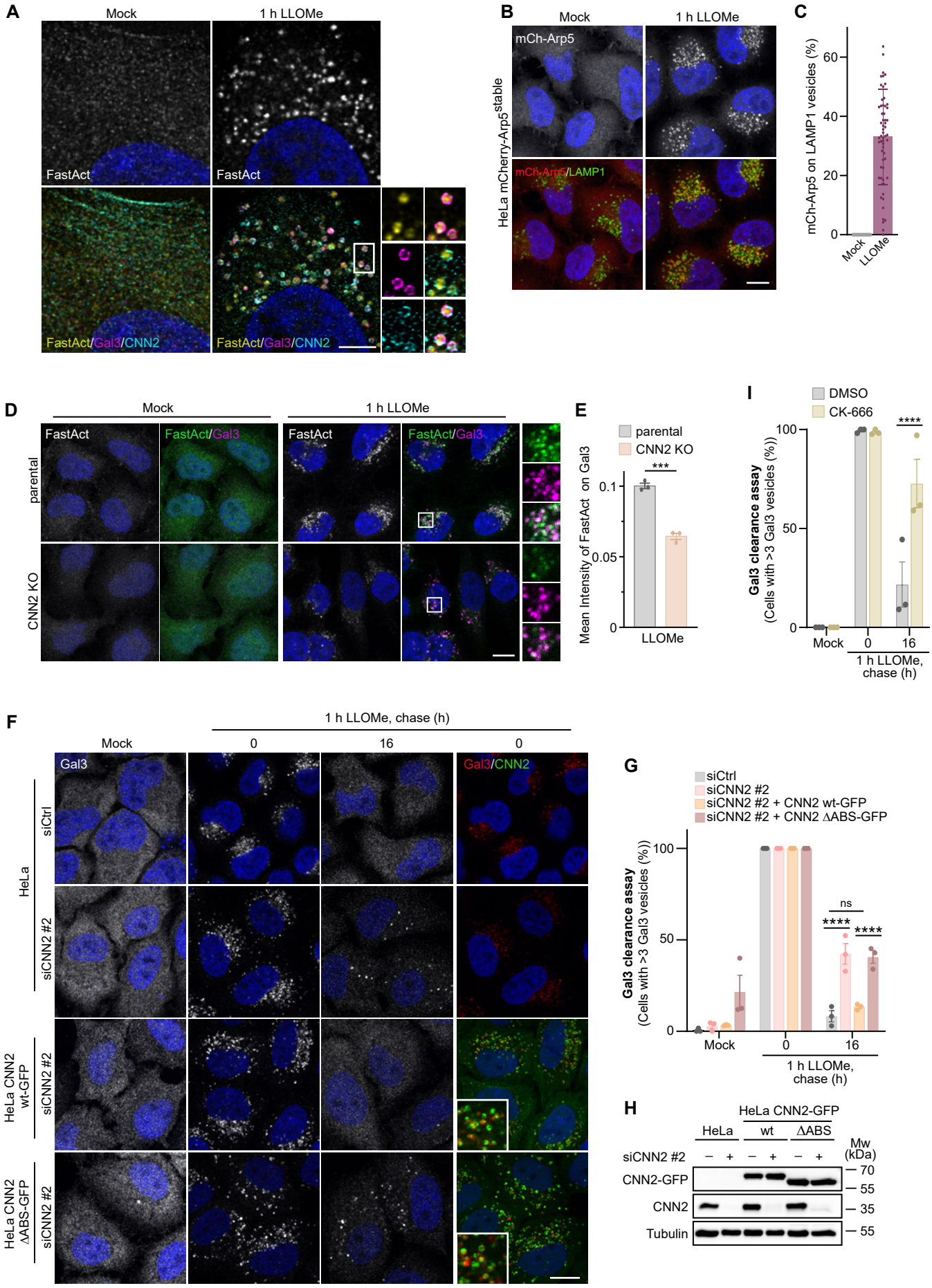
A
Mock
1 h LLOMe
FastAct
FastAct
FastAct/Gal3/CNN2
FastAct/Gal3/CNN2
B
Mock
1 h LLOMe
HeLa mCherry-Arp5stable
mCh-Arp5
mCh-Arp5/LAMP1
C
mCh-Arp5 on LAMP1 vesicles (%)
60
40
20
0
Mock
LLOMe
D
Mock
1 h LLOMe
parental
CNN2 KO
FastAct
FastAct/Gal3
FastAct
FastAct/Gal3
E
parental
CNN2 KO
***
Mean Intensity of FastAct on Gal3
0.1
0.05
0
LLOMe
I
DMSO
CK-666
Gal3 clearance assay
(Cells with >3 Gal3 vesicles (%))
100
50
0
****
Mock
0
16
1 h LLOMe,
chase (h)
F
1 h LLOMe, chase (h)
Mock
0
16
0
Gal3
Gal3/CNN2
HeLa
siCtrl
siCNN2 #2
HeLa CNN2
wt-GFP
siCNN2 #2
HeLa CNN2
ΔABS-GFP
siCNN2 #2
G
siCtrl
siCNN2 #2
siCNN2 #2 + CNN2 wt-GFP
siCNN2 #2 + CNN2 ΔABS-GFP
Gal3 clearance assay
(Cells with >3 Gal3 vesicles (%))
100
50
0
ns
****
****
Mock
0
16
1 h LLOMe,
chase (h)
H
HeLa CNN2-GFP
HeLa
wt
ΔABS
siCNN2 #2
– + – + – +
Mw
(kDa)
CNN2-GFP
70
55
CNN2
35
Tubulin
55

**Figure 3**

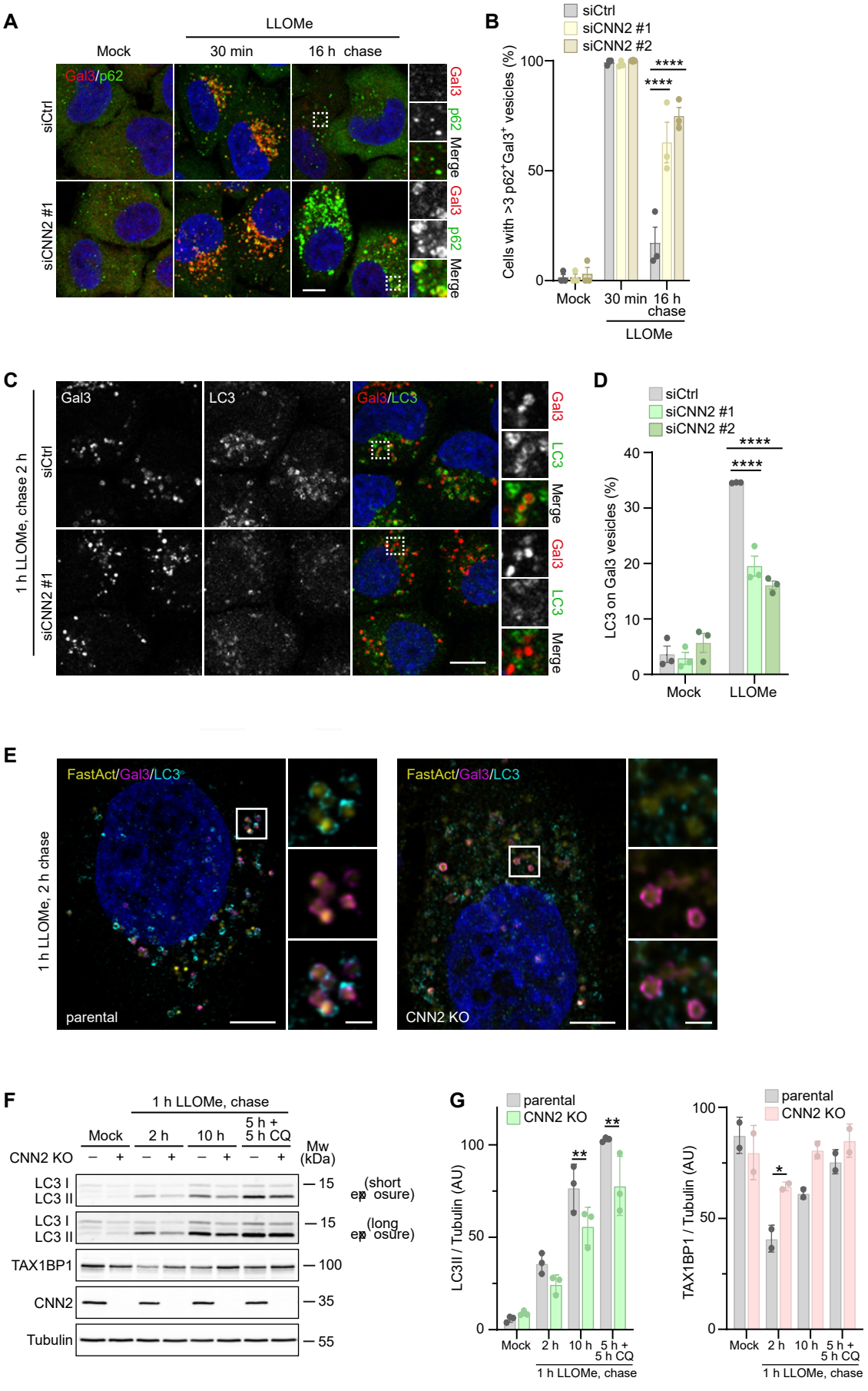
A
LLOMe
Mock
30 min
16 h chase
Gal3/p62
siCtrl
siCNN2 #1
Gal3
p62
Merge
B
siCtrl
siCNN2 #1
siCNN2 #2
Cells with >3 p62+Gal3+ vesicles (%)
100
50
0
****
****
Mock
30 min
16 h chase
LLOMe
C
1 h LLOMe, chase 2 h
siCtrl
siCNN2 #1
Gal3
LC3
Gal3/LC3
Merge
D
siCtrl
siCNN2 #1
siCNN2 #2
LC3 on Gal3 vesicles (%)
40
30
20
10
0
****
****
Mock
LLOMe
E
1 h LLOMe, 2 h chase
FastAct/Gal3/LC3
parental
CNN2 KO
F
1 h LLOMe, chase
Mock
2 h
10 h
5 h + 5 h CQ
CNN2 KO
Mw (kDa)
LC3 I
LC3 II
(short exposure)
(long exposure)
TAX1BP1
CNN2
Tubulin
15
100
35
55
G
parental
CNN2 KO
LC3II / Tubulin (AU)
TAX1BP1 / Tubulin (AU)
**
**
*
Mock
2 h
10 h
5 h + 5 h CQ
1 h LLOMe, chase

**Figure 4**

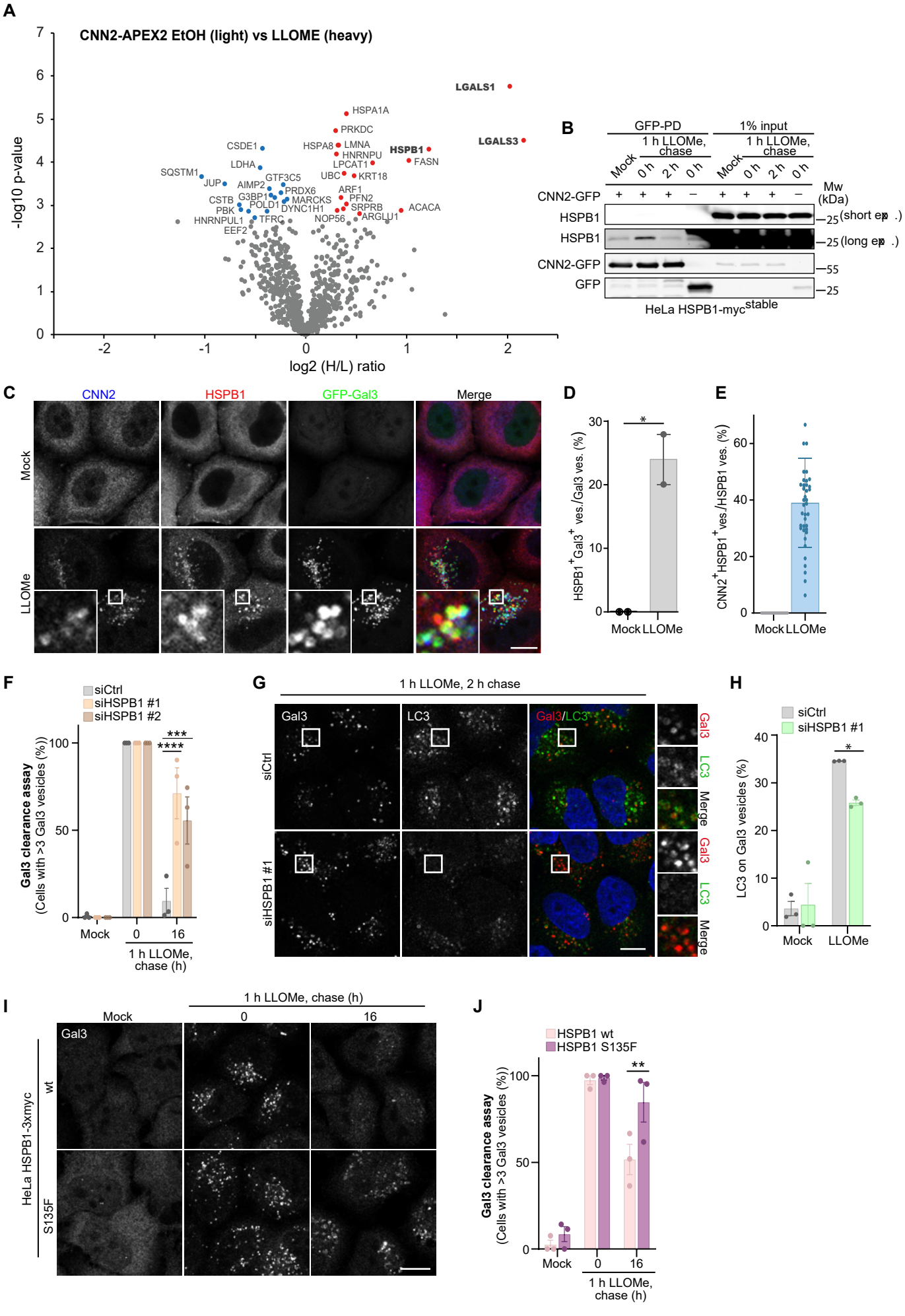
A
CNN2-APEX2 EtOH (light) vs LLOME (heavy)
-log10 p-value
log2 (H/L) ratio
LGALS1
LGALS3
HSPA1A
PRKDC
HSPB1
FASN
B
GFP-PD
1% input
1 h LLOMe, chase
Mock
0 h
2 h
0 h
CNN2-GFP
HSPB1
GFP
Mw (kDa)
HeLa HSPB1-myc stable
C
CNN2
HSPB1
GFP-Gal3
Merge
Mock
LLOMe
D
HSPB1+Gal3+ ves./Gal3 ves. (%)
E
CNN2+HSPB1+ ves./HSPB1 ves. (%)
F
siCtrl
siHSPB1 #1
siHSPB1 #2
Gal3 clearance assay
(Cells with >3 Gal3 vesicles (%))
1 h LLOMe, chase (h)
G
1 h LLOMe, 2 h chase
Gal3
LC3
Gal3/LC3
siCtrl
siHSPB1 #1
H
LC3 on Gal3 vesicles (%)
I
HeLa HSPB1-3xmyc
wt
S135F
1 h LLOMe, chase (h)
J
HSPB1 wt
HSPB1 S135F

**Figure 5**

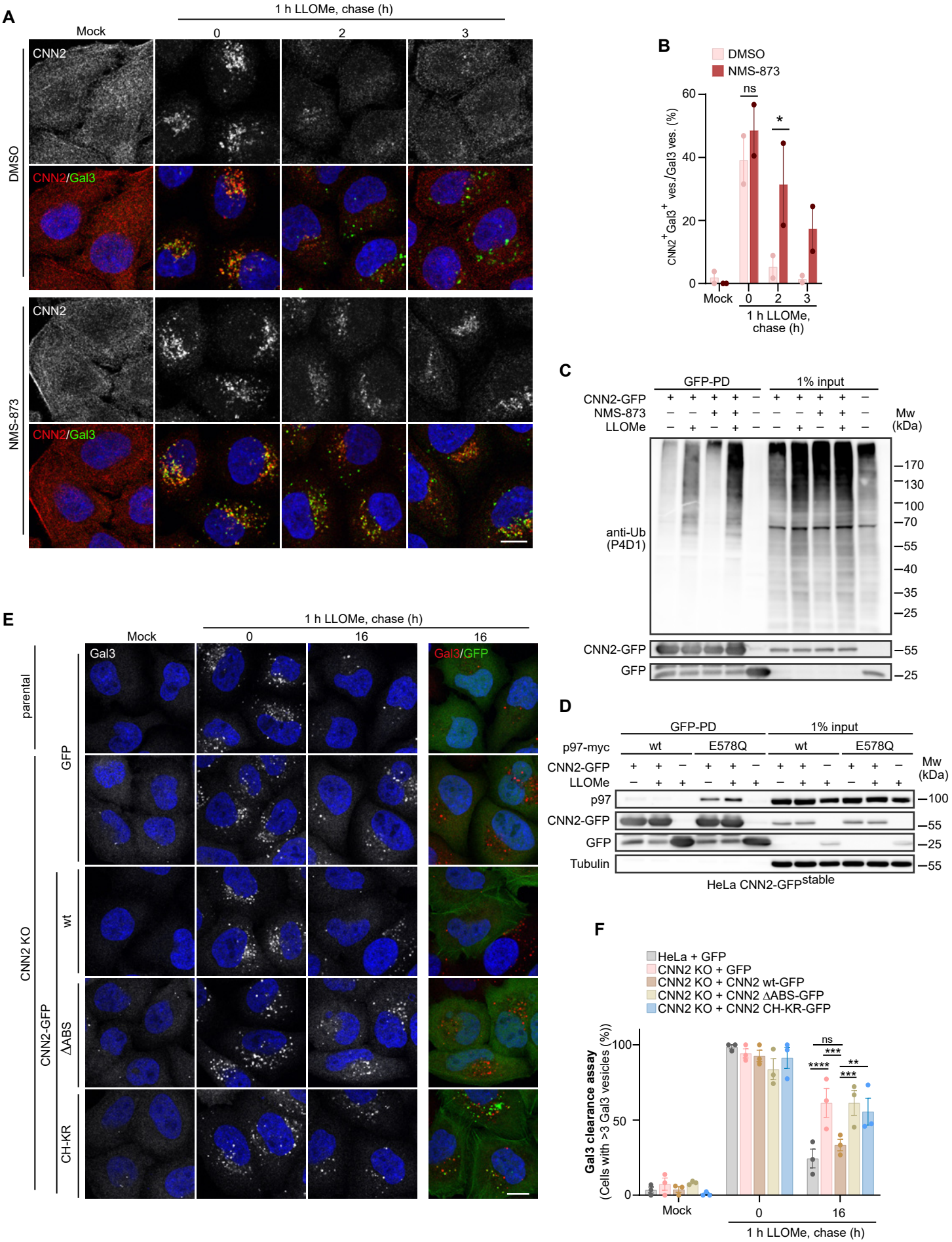
A
1 h LLOMe, chase (h)
Mock
0
2
3
DMSO
NMS-873
CNN2
CNN2/Gal3
B
DMSO
NMS-873
ns
*
CNN2+Gal3+ ves./Gal3 ves. (%)
60
40
20
0
Mock
0
2
3
1 h LLOMe, chase (h)
C
GFP-PD
1% input
CNN2-GFP
NMS-873
LLOMe
Mw (kDa)
anti-Ub (P4D1)
170
130
100
70
55
40
35
25
CNN2-GFP
GFP
D
GFP-PD
1% input
p97-myc
wt
E578Q
wt
E578Q
CNN2-GFP
LLOMe
Mw (kDa)
p97
CNN2-GFP
GFP
Tubulin
100
55
25
55
HeLa CNN2-GFPstable
E
1 h LLOMe, chase (h)
Mock
0
16
16
parental
CNN2 KO
GFP
CNN2-GFP
wt
ΔABS
CH-KR
Gal3
Gal3/GFP
F
HeLa + GFP
CNN2 KO + GFP
CNN2 KO + CNN2 wt-GFP
CNN2 KO + CNN2 ΔABS-GFP
CNN2 KO + CNN2 CH-KR-GFP
Gal3 clearance assay (Cells with >3 Gal3 vesicles (%))
100
50
0
ns
***
****
**
***
Mock
0
16
1 h LLOMe, chase (h)

**Figure 6**

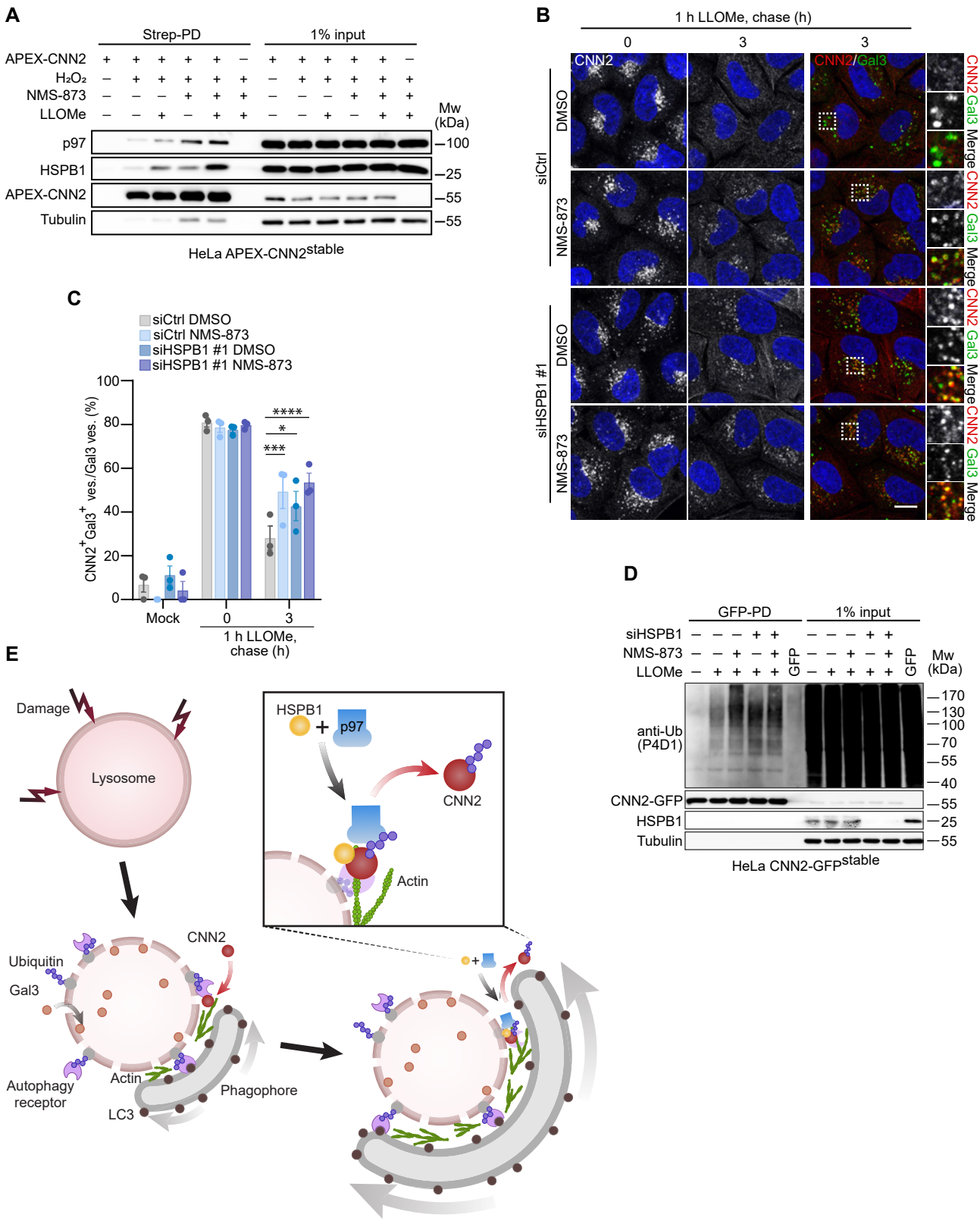
A
Strep-PD
1% input
APEX-CNN2
H2O2
NMS-873
LLOMe
Mw (kDa)
p97
HSPB1
APEX-CNN2
Tubulin
100
25
55
55
HeLa APEX-CNN2stable
B
1 h LLOMe, chase (h)
0
3
3
CNN2
CNN2/Gal3
siCtrl
siHSPB1 #1
DMSO
NMS-873
CNN2 Gal3 Merge
C
siCtrl DMSO
siCtrl NMS-873
siHSPB1 #1 DMSO
siHSPB1 #1 NMS-873
CNN2+Gal3+ ves./Gal3 ves. (%)
Mock
1 h LLOMe, chase (h)
D
GFP-PD
1% input
siHSPB1
NMS-873
LLOMe
GFP
Mw (kDa)
anti-Ub (P4D1)
CNN2-GFP
HSPB1
Tubulin
HeLa CNN2-GFPstable
E
Damage
Lysosome
HSPB1
p97
CNN2
Actin
Ubiquitin
Gal3
Autophagy receptor
LC3
Phagophore

**Figure 7**

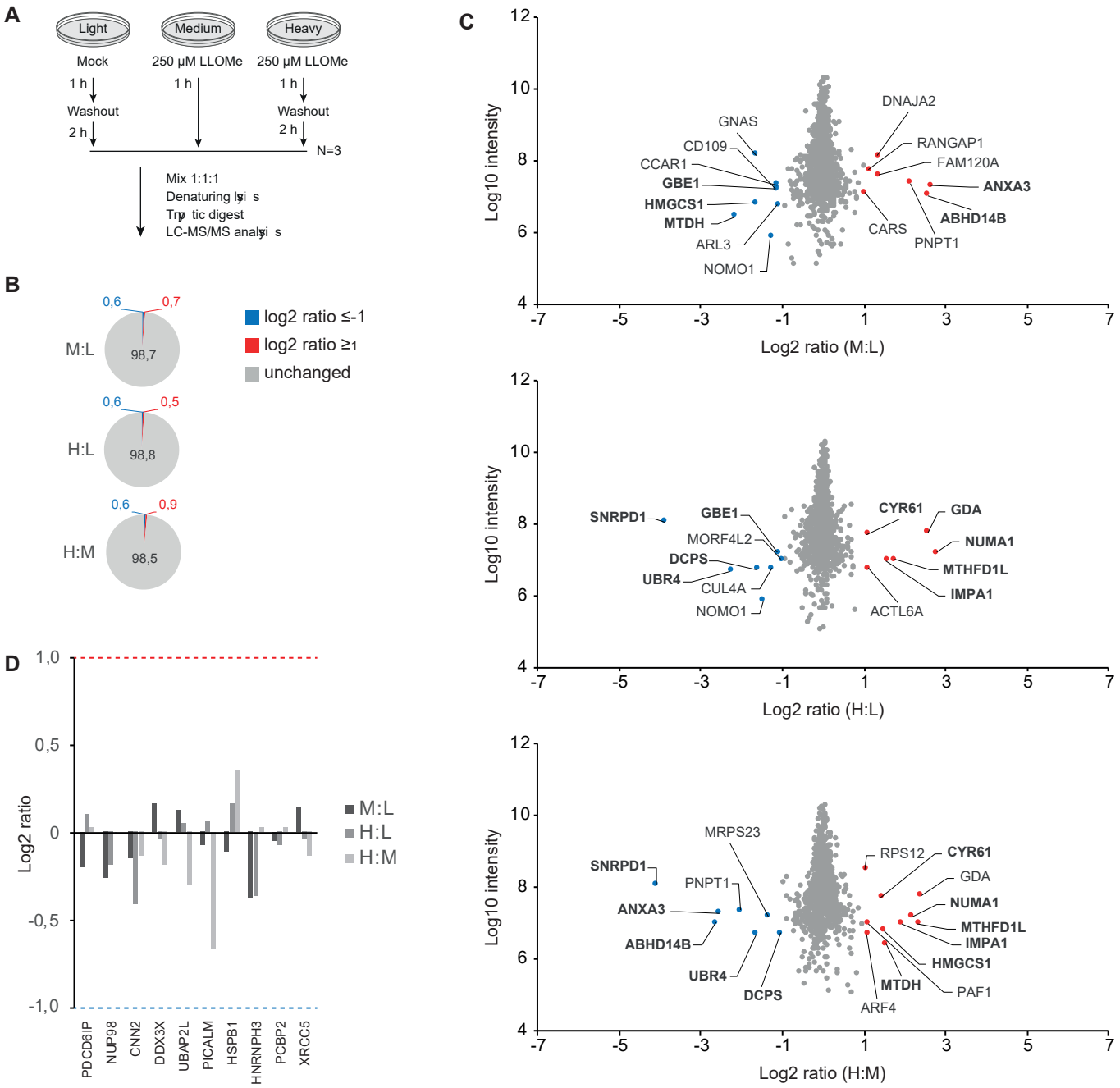


**Supplementary Figure 1 - related to Figure 1**

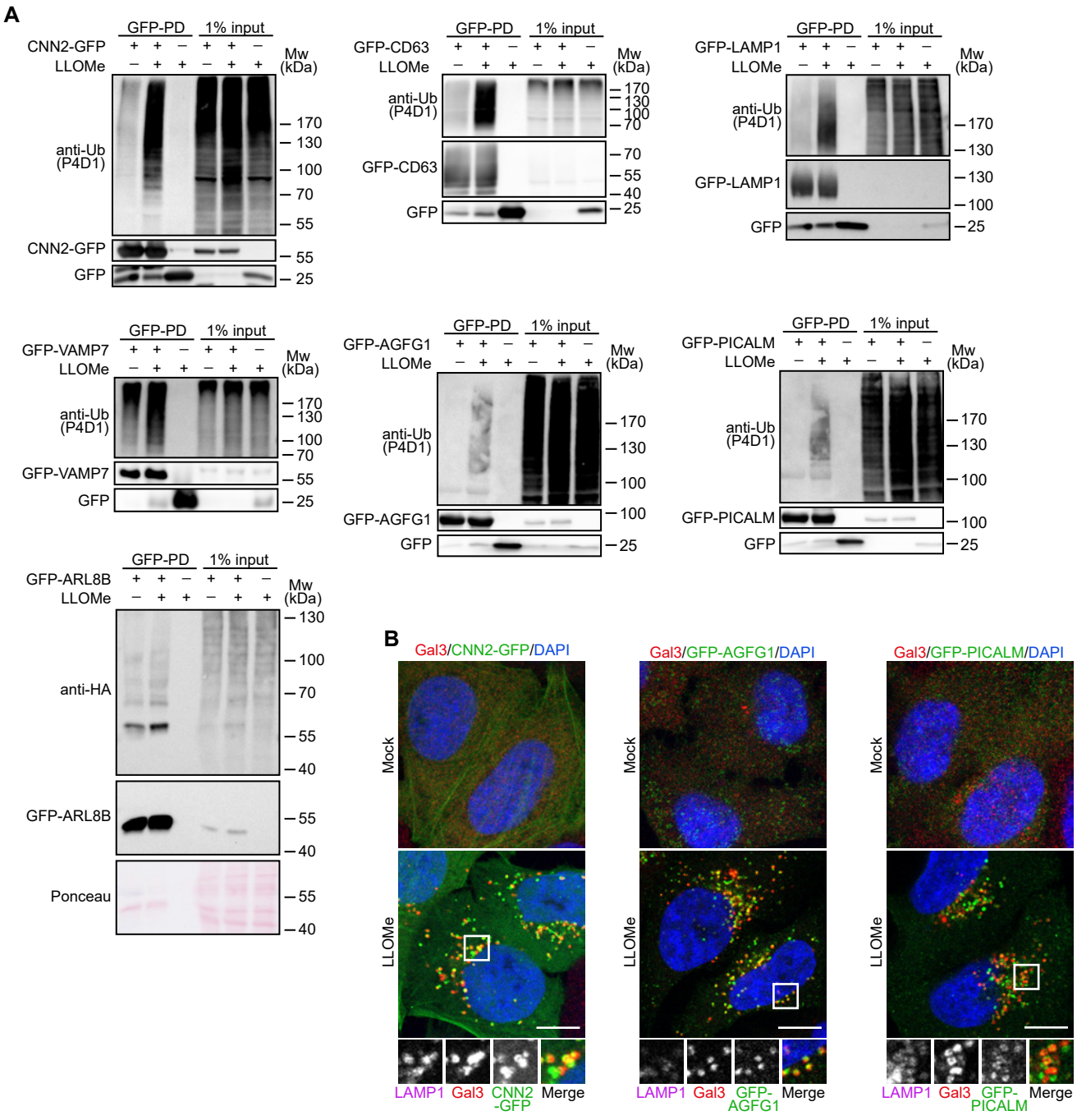


**Supplementary Figure 2 - related to Figure 1**

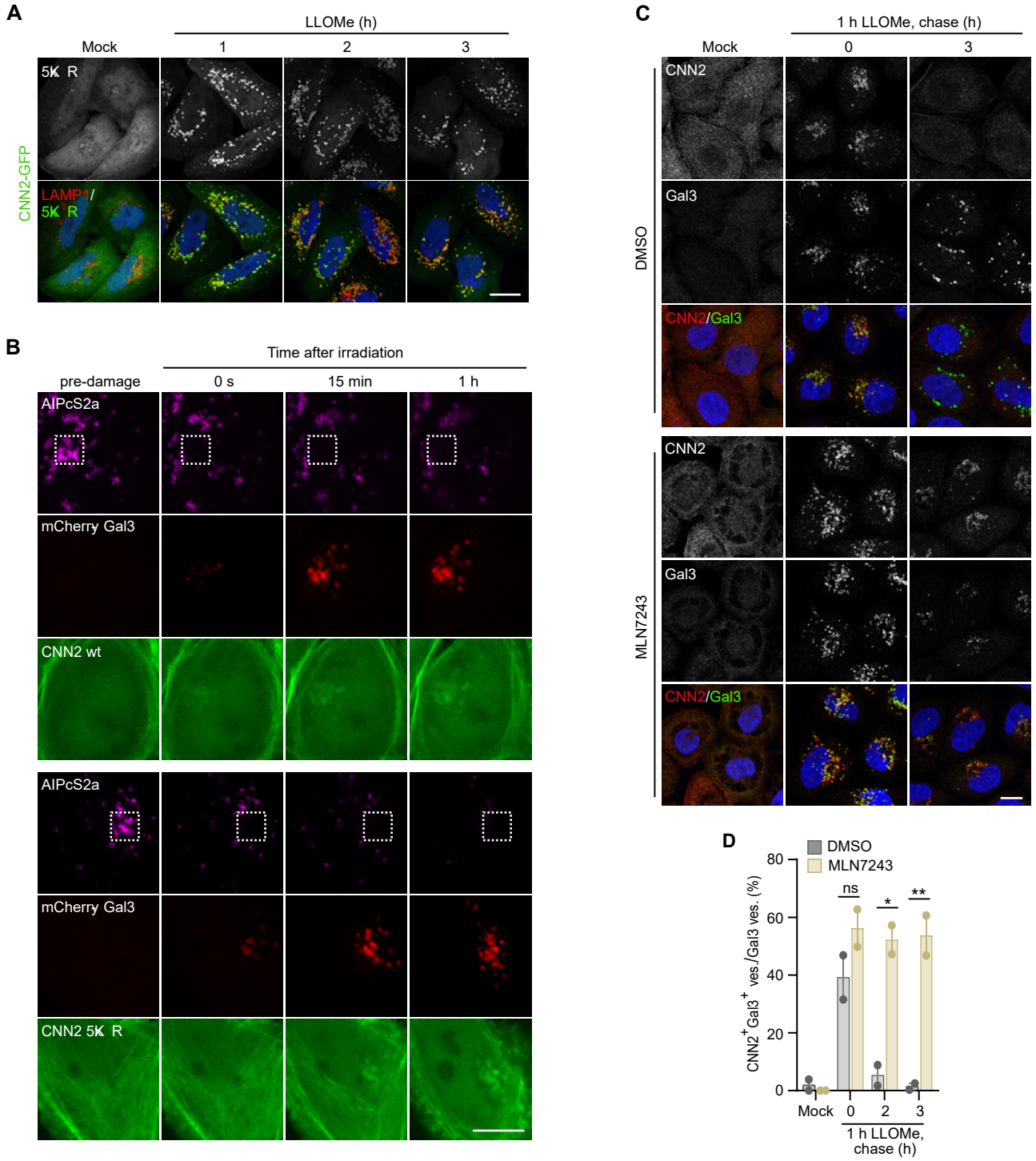


**Supplementary Figure 3 - related to Figure 2**

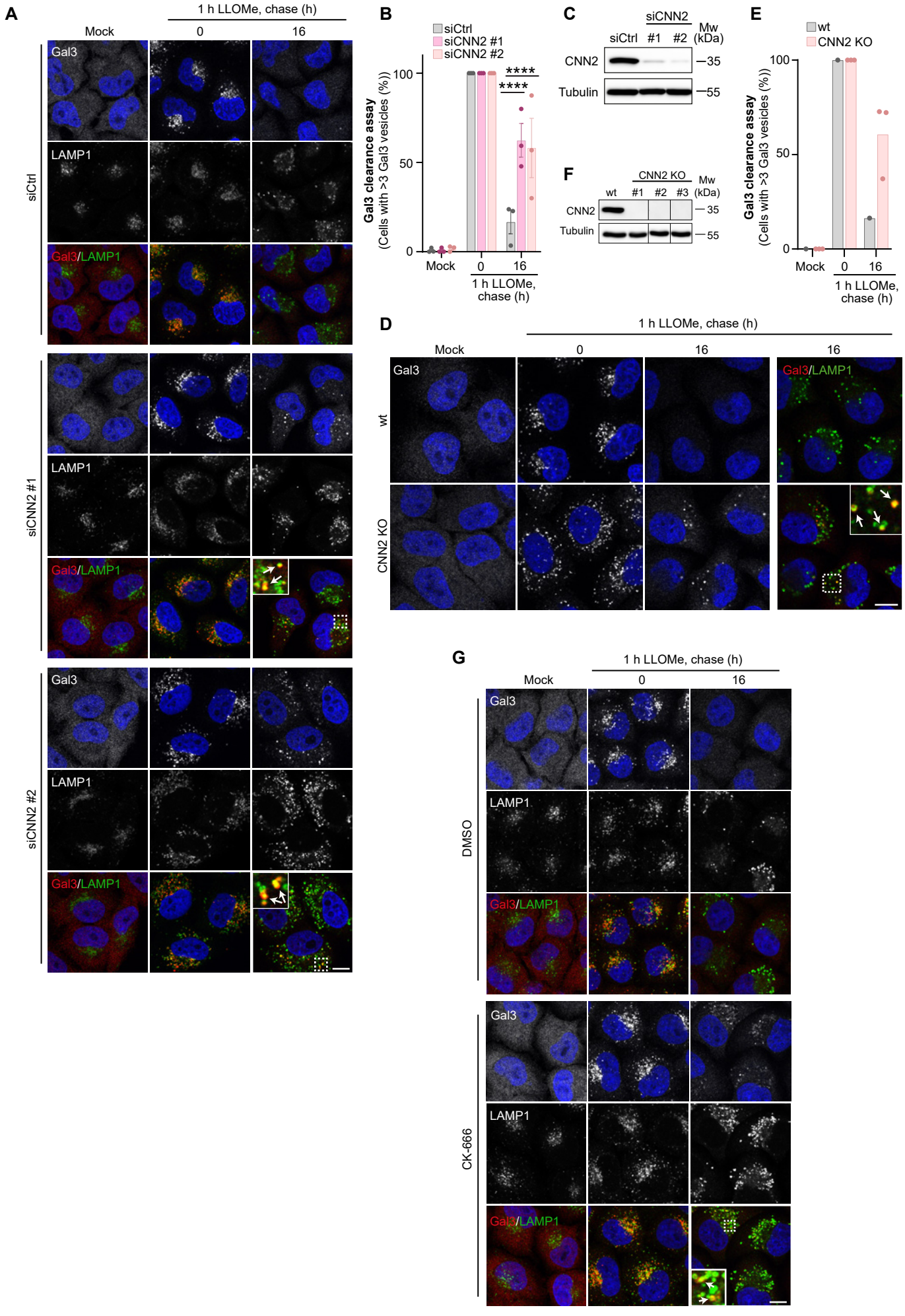


**Supplementary Figure 4 - related to Figure 3**

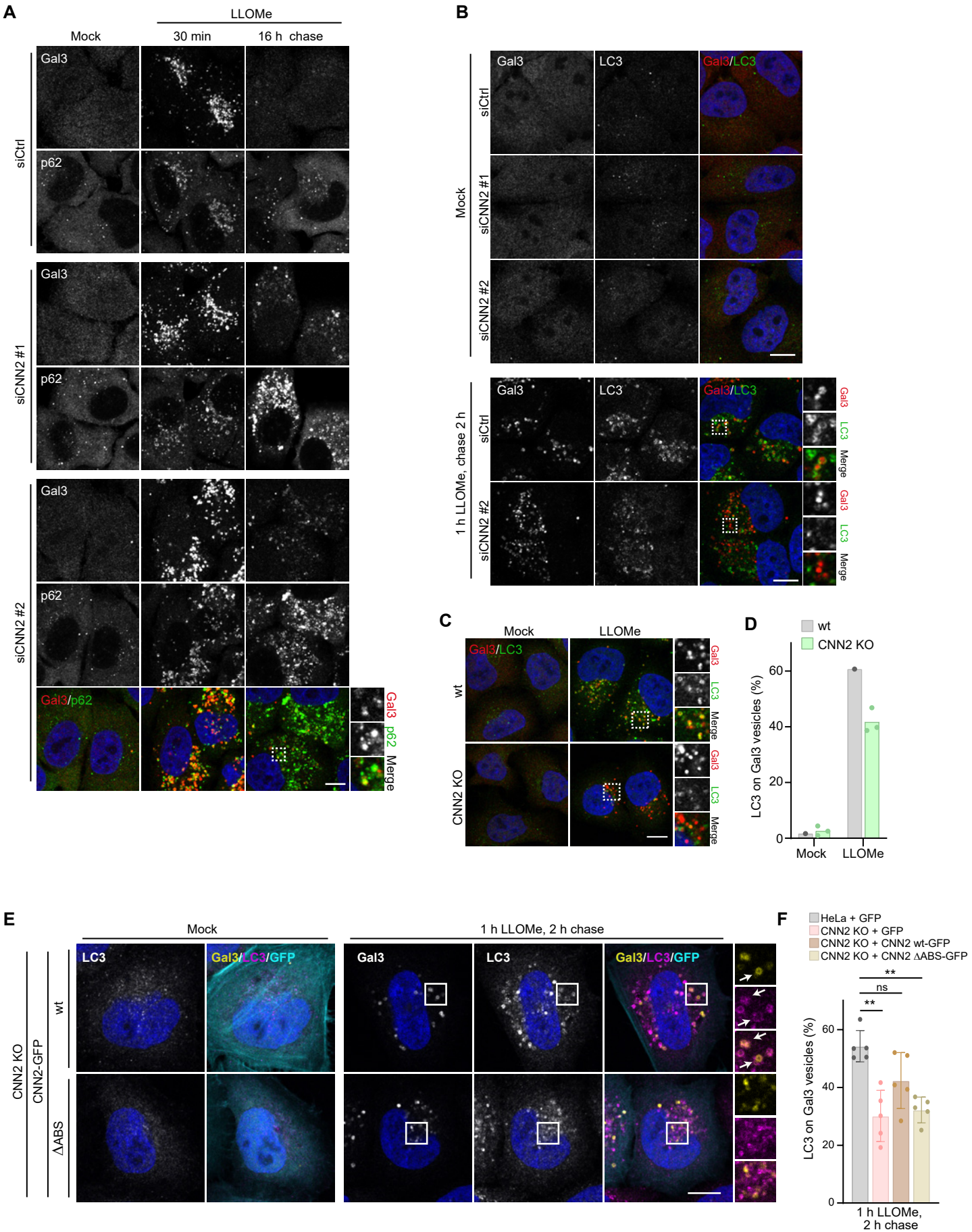


**Supplementary Figure 5 - related to Figure 4**

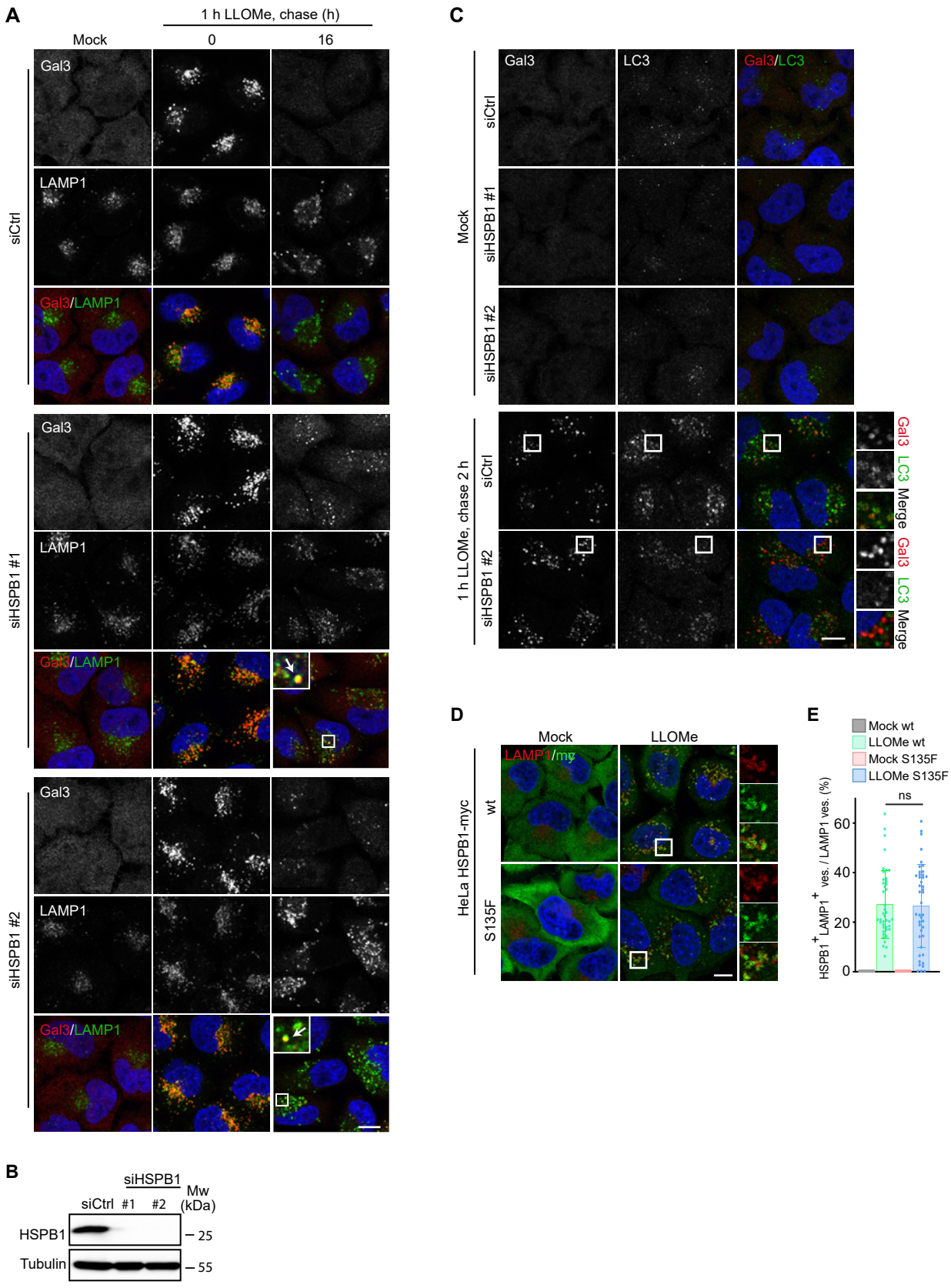


**Supplementary Figure 6 - related to Figure 5**

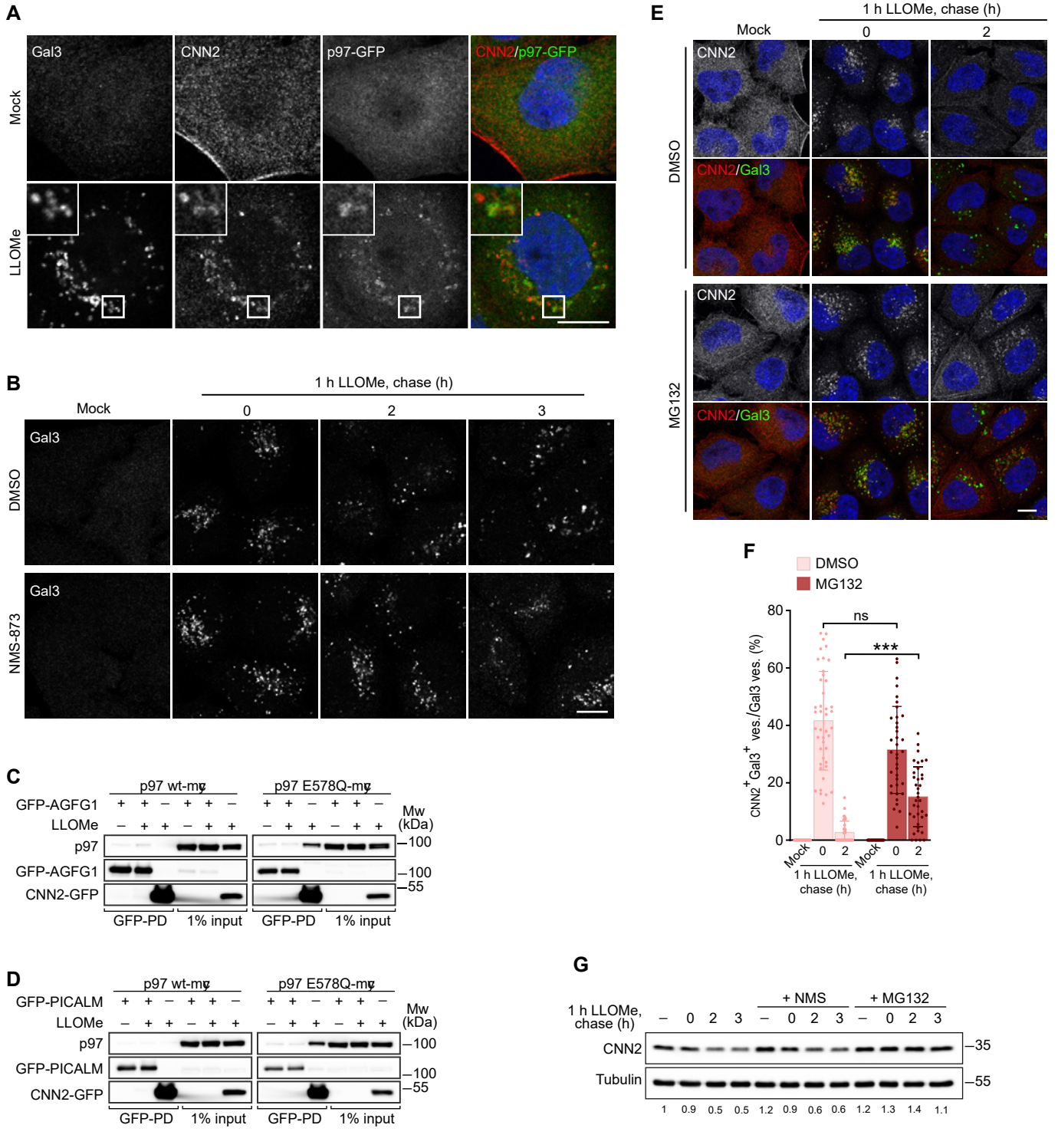


**Supplementary Figure 7 - related to Figure 6**

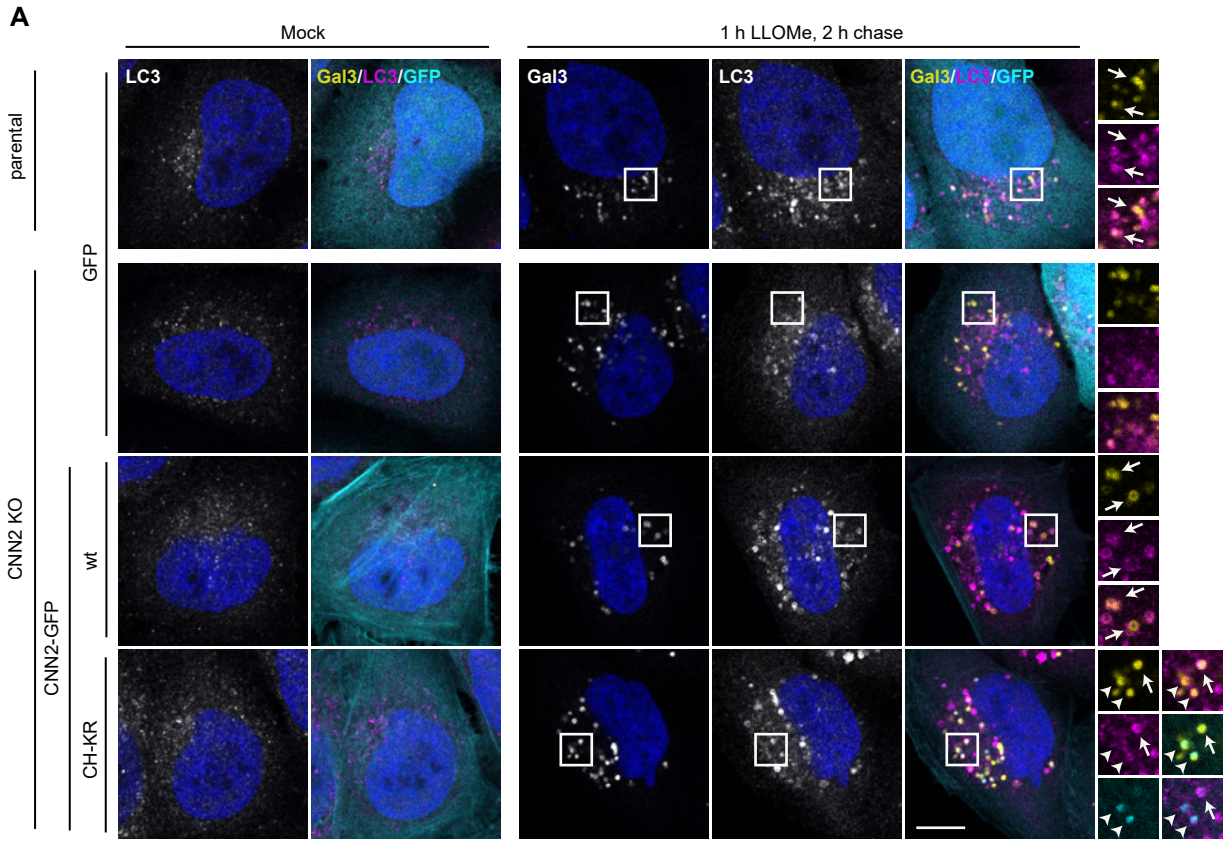


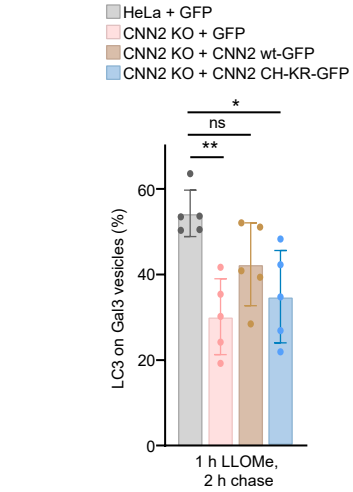


**Supplementary Figure 8 - related to Figure 6**

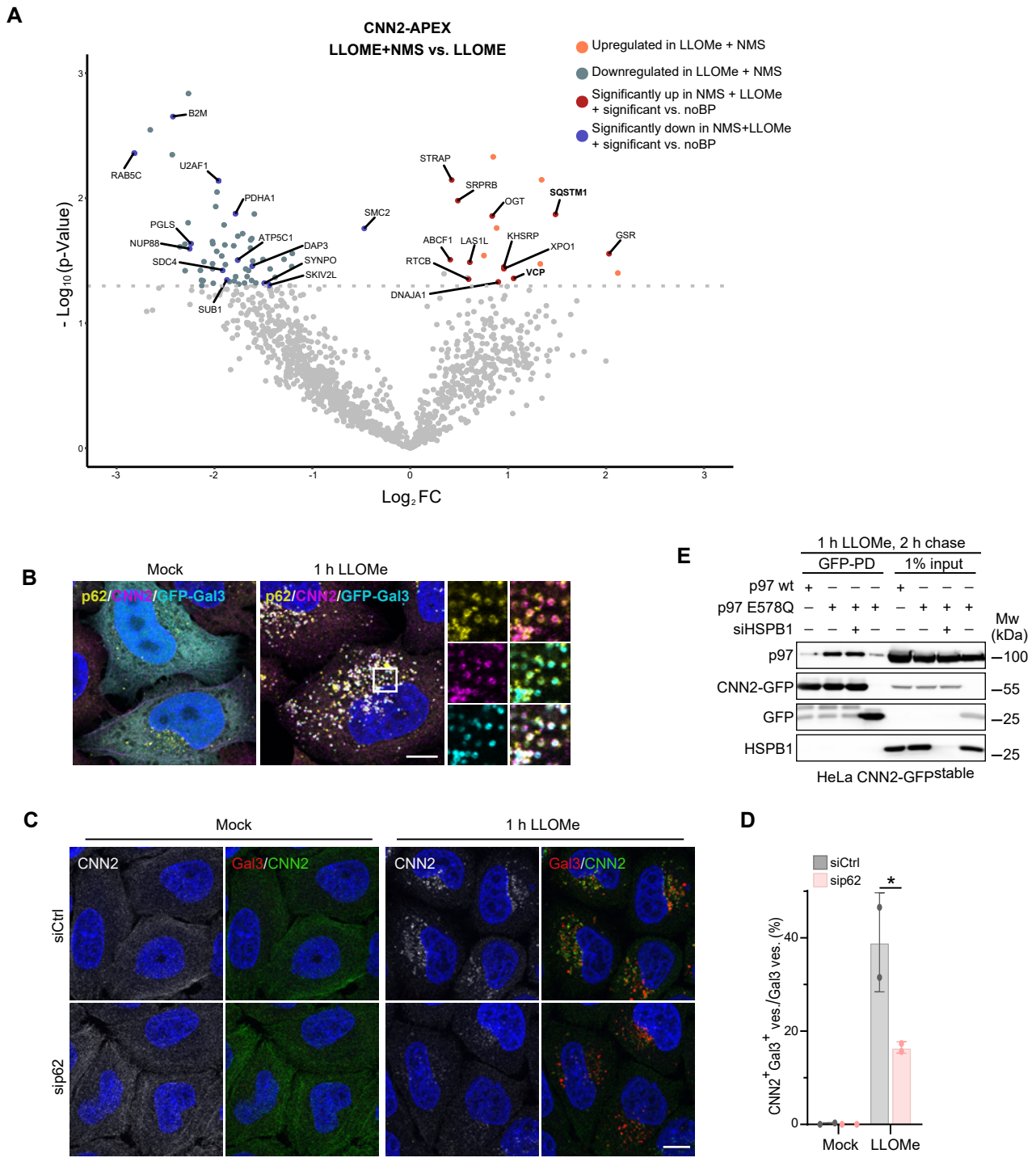


**Supplementary Figure 9**